T H E U N I V E R S I T Y O F M I C H I G A N

COLLEGE OF LITERATURE, SCIENCE, AND THE ARTS
Department of Physics

Technical Report No. 19

HIGH ENERGY π^- + p ELASTIC SCATTERING FOR SMALL MOMENTUM TRANSFERS AND FORWARD DISPERSION CALCULATIONS

Howard I. Saxer

ORA Project 03106

under contract with:

DEPARTMENT OF THE NAVY
OFFICE OF NAVAL RESEARCH
CONTRACT NO. Nonr-1224(23)
WASHINGTON, D.C.

administered through:

OFFICE OF RESEARCH ADMINISTRATION ANN ARBOR

December 1964

This report was also a dissertation submitted in partial fulfillment of the requirements for the degree of Doctor of Philosophy in The University of Michigan, 1964.

ACKNOWLEDGMENTS

I would like to express my sincere gratitude to Professor Lawrence W. Jones for the guidance he gave me throughout the course of the work presented in this thesis.

I am equally indebted to Professor Martin L. Perl for suggesting this work and for his continued interest and advice.

I am grateful to Professor C. C. Ting, Dr. D. E. Damouth, Dr. K. W. Lai, Dr. R.Y.Y. Lee, and Mr. O. Haas for their help in the design, setup, and execution of the experiment and for their valuable suggestions in the analysis of the data.

I also wish to acknowledge the enthusiastic support of Dr. E. J. Lofgren, his colleagues, and the staff of the Bevatron of the Lawrence Radiation Laboratory.

Mr. S. Thomas Shibuta deserves special acknowledgment for his valuable assistance in the data analysis and dispersion calculations.

Finally, I express my deep appeciation to Miss Marion Becker, Miss Carol McGhee, Mrs. Mary E. Baird, and Mrs. Jeannette Currier for their assistance.

TABLE OF CONTENTS

TABLE OF CONTENTS (Concluded)

LIST OF TABLES

LIST OF FIGURES

ABSTRACT

The negative pion-proton elastic differential cross section was measured at incident pion momenta of 2.01, 3.15, 4.13, and 4.95 BeV/c for the range of the square of the four momentum transfer of $.0008 \leq |t| \leq .154$ $(\text{BeV/c})^2$.

The data extended into the region where Coulomb scattering contributions were significant. Experimental values for the real part of the forward nuclear scattering amplitude were calculated using a simple interference model for Coulomb nuclear interaction. The best values found are consistent with dispersion theory predictions in that the sign is negative, indicating destructive interference.

Forward dispersion relation calculations were carried out for pion kinetic energies of 1 to 29 BeV using recent $\pi^{\pm}$ + p total cross section results.

INTRODUCTION

This experiment is one of three related spark chamber experiments, which were run in succession, designed to investigate the π^-+p elastic differential cross sections for 2-5 BeV/c. The experiments of Damouth, Perl, and Jones[1] at 2 BeV/c and Perl, Jones, and Ting[2] for 3-5 BeV/c were concerned with large momentum transfers in elastic π^-+p scattering. This experiment is concerned with the range of the square of the four momentum transfer $.0008 \leq |t| \leq .15$ $(BeV/c)^2$ for laboratory pion momenta of 2.01, 3.15, 4.13, and 4.95 BeV/c. The intent was to study the nuclear diffraction peak. The results presented are consistent with the other two experiments.

For 2-4 BeV/c the data of this experiment extended into the region where Coulomb scattering was significant. This allowed a direct calculation of the real part of the forward nuclear scattering amplitude for a simple interference model.

These results are presented along with theoretical calculations of the real part of the forward scattering amplitude from dispersion relations in the light of recent total cross section data. These calculations were made for 1-29 BeV pion kinetic energy.

CHAPTER I

EXPERIMENTAL SETUP

The experiment to be described here was run at the Bevatron of the Lawrence Radiation Laboratory. The objective was to find elastic differential cross sections for π^-+p at small momentum transfers ($.0008 \leq |t| \leq .15$ $(\text{BeV/c})^2$). The experiment was carried out for incident laboratory pion momenta of 2.01, 3.15, 4.13, and 4.95 BeV/c. The π^- beam was produced in the Bevatron. The beam was momentum analyzed and focused onto a hydrogen target by a series of five magnets. Selection of events was achieved by an array of scintillation counters. Four spark chambers visually reproduced segments of the pion trajectory. These were recorded on film through a system of mirrors and lenses. Additional information on the setup to what follows below is available from two related experiments immediately preceding this one.[1-4]

A. Beam and Magnets

Figure 1 shows the beam layout. The internal 6 BeV proton beam circulating in the Bevatron struck a copper target. Negative particles produced in the interaction were deflected outward by the magnetic fringe field of the Bevatron and passed through a thin window in the vacuum tank. Negative pions of a desired momentum were extracted and focused onto the hydrogen target by a series of five magnets whose cur-

rents were set by wire orbit data. Already partially momentum analyzed by the Bevatron's field, the beam was bent by two C magnets through two quadrupole triplets with an 8-in. aperture, which focused the beam. An H magnet performed the principal momentum analysis.

Leaving the H magnet, the pion beam passed through a beam telescope consisting of scintillation counters C_{12}, C_{10}, and C_{11} which had diameters of 4 in., 4 in., and 2 in., respectively. A coincidence trigger was required from these counters for a pion to be useful for the experiment.

Pions so selected by the magnets and the beam telescope formed a beam with 2-in. diameter cross section, a maximum divergence of ±1° with respect to the beam axis, and a momentum spread of less than 5% at the entry to the hydrogen target.

B. Hydrogen Target

The hydrogen target is shown in Fig. 2. A cylindrical .007 in. mylar bag, 18 in. long and of diameter 3.5 in., contained liquid hydrogen at atmospheric pressure. The bag was suspended with its axis along the beam axis. A radiation barrier consisting of 20 alternate layers of .0005 in. aluminized mylar and .001 in. aluminum foil surrounded the mylar bag with an opening left for beam entry. The contents were enclosed in a .032 in. aluminum vacuum chamber.

C. Event Detection

For the four momentum transfers considered the scattered proton subtended an angle almost perpendicular to the incident pion and, in general, did not have sufficient energy to emerge from the hydrogen target and anticoincidence scintillation counters surrounding the target. Thus,detection of elastic scatters by requiring coplanarity was not feasible. The following detection design was used:

1. Pion tracks were observed using spark chambers.
2. Inelastic and large momentum transfer events were deleted by anticoincidence counters.

The azimuthal acceptance of scattered pions was limited at the smaller angles by the beam distribution, and at the larger angles by the spark chambers and anticoincidence counters. This is discussed in Chapter III-A.

D. Spark Chambers

Four spark chambers were used for this experiment. Each spark chamber had six gaps. The spark chambers were constructed of .001 in. hardened aluminum foil plates cemented between 3/8 in. lucite frames. Alternate plates were connected externally to two electrodes, one grounded, the other pulsed to between 10 and 15 kV.

Figure 3 is a plan view of the locations of the spark chambers and scintillation counters. The two small spark chambers had 4x4 in.

plates (usable area). They were placed in front of the hydrogen target to define the angle of the incident track of the pion. Their separation was 28 3/8 in. between centers. The large chambers had usable area of 8x18 in. and were separated by 29 1/8 in. between centers. They defined the scattered track of the pion.

Neglecting all measuring effects except the intrinsic widths of the tracks as determined by the sparks, the spark chamber setup provided for measurement of scattering angles to better than 1 milliradian.

E. Counters

In addition to the beam telescope, counter A_1 was used in anticoincidence to cut down on accidental events. A_1 was a scintillation counter with a 2-in. diameter hole in the middle to allow the beam to pass through. It was placed behind the second beam defining spark chamber.

Anticoincidence counters C_{20} and C_{21} were semi-cylindrical sections surrounding the target. C_{22} fit over the front of the target with an opening for beam entry.

For larger momentum transfers the proton would come out of the target and trigger the anticoincidence counters C_{20} or C_{21}. Inelastic events producing charged particles coming off in other than forward directions would again trigger these counters. Three eighths of an

inch of lead was placed in front of C_{20}, C_{21}, and C_{22} to convert γ rays from π°'s due to inelastic events and to increase the range of elastically scattered protons, i.e., to increase the magnitude of the allowable momentum transfers. This design was chosen with the hope that the contribution of the small angle background would then be small in comparison to the π^{-}+p elastic scatters.

One additional anticoincidence counter, A_4, was placed 6.3 ft beyond the last spark chamber and centered on the beam axis to eliminate unscattered events. A_4 was a circular scintillation counter with diameter 7.25 in.

A block diagram of the trigger system is shown in Fig. 4. An event was recorded for each trigger of the beam telescope with no accompanying trigger of any anticoincidence counter.

F. Optics and Camera

Through a system of front-silvered mirrors the direct and stereo views of all the spark chambers were brought down onto a 54 in. square mirror, inclined at 45°, which directed the views to the cameras. To avoid depth distortion the image of the views of the two central spark chambers passed first through a 36 in. diameter 30 ft focal length plastic field lens. Two Beattie-Coleman cameras, using 1 ft focal length lenses, were located about 30 ft from the center spark chambers. Each event was recorded on a double sized frame (1-1/2 in. long) of 35

mm film, giving an overall reduction of 30 to 1. The "A" camera looked directly at the system and was set up to take only one event per Bevatron pulse, while the "B" camera picked up the remainder on one frame. Only the events from the "A" camera were analyzed.

Each frame contained an identification number, eight spark chamber views, and a fiducial grid for reference.

The mirror for the stereo view of the first downstream spark chamber was approximately 1 in. too short, so that the effective area of this chamber was too small. This was compensated for in solid angle corrections (Chapter III-A).

CHAPTER II

ANALYSIS OF DATA

Over 25,000 frames were taken with the "A" camera. A visual scanning procedure was set up to select good events. Coordinates defining the tracks were measured from a scanning machine. These data were then run in a computer program which reconstructed the events.

A. Selection Procedure

A selection procedure was adopted to distinguish good events from background. Good events were defined as having clear tracks so that measurements would be reproducible and as having intersections which took place between the two center spark chambers. A comprehensive classification of all 25,000 frames was made. Each frame was classified at least twice. The results of the second classification were compared with the first classification. Those frames not classified the same were re-examined.

An adjustment of normalization was made for the loss of elastic events in order to find the number of incoming pions associated with the number of elastic scatters found. A detailed classification was set up to give a comprehensive understanding of good events as well as background events and to account for the loss of those events which could not be accurately measured.

1. CATEGORIES

Each frame was projected onto a viewing screen and from observation was placed in one of five categories.

a. N—Some random effect occurred which made it impossible to measure the frame regardless of its contents, i.e., the frame was overexposed, underdeveloped.

b. P—By virtue of the type of event, part of the event blanked out, thus making it impossible to categorize it as H, L, or T. For example, the pion underwent a large angle scatter and missed the last chamber.

c. H—All four spark chambers had clear definite tracks. Each spark chamber had at least two sparks with a separation of at least two gaps.

d. L—By virtue of the event, it was evident that one or more spark chambers misfired.

e. T—The same as H except that the event looked inelastic because of the presence of two or more scattered particles. At least one of these particles must have made it through both downstream spark chambers.

The order of preference in categorizing was to check for N types, then P types, otherwise H, L, or T types. Each of these five categories had several subcategories.

2. NORMALIZATION

Had the events been visible, the number of frames of the P category, $N_{P'}$, which would have been in the H and T categories is

$$N_{P'} = \frac{(N_H + N_T)}{(N_H + N_T + N_L)} N_P$$

where N_H is the number of frames in the H category, etc. The total normalization, N, corrected for the loss of elastic events due to spark chamber misfirings is then

$$N = (N_H + N_T + N_{P'})/(E/B) - \frac{N_{P'}}{N_P} N_{PS} \qquad (1)$$

where (E/B) is the event to beam ratio and N_{PS} is the number of skew particles which did not come from the beam. These almost always fell into the P category by virtue of their divergence from the beam axis.

The loss of elastic events due to the blanking of events (P category) was compensated for in solid angle corrections.

B. Measuring

The measuring was done on two types of scanning machines, one manual and the other digitizing. Both machines projected the film image onto emulsion screens, but the measuring was carried out in different ways.

The manual machine was set up to take measurements on the image. A ruled mask with openings cut away for spark chamber views, fiducials,

and frame number was fixed to the screen. Adjustment knobs on the machine allowed the operator to move the screen in the image focal plane. The screen was lined up with the fiducials of the image. The operator would line up a straight edge along the spark tracks to a best visual fit and record the coordinate of the intersection of the straight edge with the mask. The data were later punched on IBM cards. The coordinates were read to the nearest 1/2 mm on the mask. The image was about 2/3 of the actual size so that the individual measurements were accurate to 3/4 mm. Actually the accuracy was less than this primarily due to errors in lining up the fiducials, and also due to distortions from film shrinkage and the optical system of the scanning machine.

Measurements on the digitizing machine were made with respect to the optical axis. An image of a cross hair appeared on the screen to mark this axis. The operator had controls to rotate the cross hair and to move the film carriage so as to line up any point with the image of the cross hair. The shift of the carriage was accurately digitized to 8,000 counts per inch both along the length and width of the film. The film was held down by a partial vacuum. The operator recorded the coordinates of a point lined up with the center of the cross hair on IBM cards automatically by the push of the record button. By recording two fiducial points and one point along each of the tracks in the eight spark chamber views, the event was completely determined.

The coordinates of each point on the film were reproducible to 2/8000 of an inch. Thus an overall limit to the accuracy of a measured

point scaled to the actual size of the experiment was found to be about .3 mm.

All the frames were measured at least twice on the manual scanning machine. If the results were contradictory, the frame was remeasured as many times as needed until consistent results were obtained.

To achieve more accuracy for 2.01 and 3.15 BeV/c, the elastic scatter events found from the manual scan were remeasured on the digitizing machine.

Six people were employed to carry out the manual measuring. Four were experienced scanners and did the bulk of the measurements.

Accuracy checks were made by direct comparison of the two independent measurements and errors were corrected by remeasurement.

C. Event Calculations and the Parameters

1. EVENT CALCULATIONS

Because of competing small angle scatters from materials outside the target, the accurate location of the point of interaction was important.

Due to truncation in measurements, finite spark widths, etc., the beam track did not intersect the scattered pion track. Therefore the intersection was defined to be the average of the end points of the perpendicular line segment joining the two tracks. The length of this segment was the minimum distance between the tracks.

From Fig. 5, $\vec{D}$ is the directed distance of the perpendicular line segment from the scattered track to the beam track; $\vec{a}$ is the direction cosine vector of the beam track and $\vec{X}_o$ is a vector to any point on the track; $\vec{A}$ is the direction cosine vector of the scattered track and $\vec{X}_1$ is a vector to any point on the track; $\vec{X}_B$ and $\vec{X}_S$ define the end points of $\vec{D}$.

$$\vec{X}_B = \vec{X}_o + \vec{R} = \vec{X}_o + |R|\vec{a} \tag{2}$$

$$\vec{X}_S = \vec{X}_1 + \vec{S} = \vec{X}_1 + |S|\vec{A} \tag{3}$$

$$\Delta\vec{X} = \vec{X}_1 - \vec{X}_o \tag{4}$$

$$\Delta\vec{X} = \vec{R} - \vec{D} - \vec{S} \tag{5}$$

Taking successively the dot product of $\vec{A}$ and $\vec{a}$ with Eq. (5)

$$\vec{A}\cdot\Delta\vec{X} = |R| \cos\theta - |S| \tag{6}$$

$$\vec{a}\cdot\Delta\vec{X} = |R| - |S| \cos\theta \tag{7}$$

$$\vec{A}\cdot\vec{a} = \cos\theta \tag{8}$$

$$\vec{A}\cdot\vec{D} = \vec{a}\cdot\vec{D} = 0$$

Solving for $|R|$ and $|S|$ from Eqs. (6) and (7), and substituting into Eqs. (2) and (3)

$$\vec{X}_B = \vec{X}_o + \left[\frac{\vec{a}\cdot\Delta\vec{X}\cos\theta - \vec{A}\cdot\Delta\vec{X}}{1 - \cos^2\theta}\right]\vec{a} \tag{9}$$

$$\vec{X}_S = \vec{X}_1 + \left[\frac{\vec{a}\cdot\Delta\vec{X} - \vec{A}\cdot\Delta\vec{X}\cos\theta}{1 - \cos^2\theta}\right]\vec{A}. \qquad (10)$$

For this experiment $(\vec{X}_B+\vec{X}_S)/2$ was used for the intersection of an event, and the scattering angle was found from Eq. (8).

With the Z axis picked as the beam axis, the numerators in the brackets in Eqs. (9) and (10) for small angles go as

$$[\vec{a}\cdot\Delta\vec{X} - \vec{A}\cdot\Delta\vec{X}]$$

where $(a_X, a_y, A_X, A_y) \ll \epsilon < 1$

$$a_Z \sim A_Z \sim 1 - \epsilon \ .$$

For $\Delta Z \sim \Delta X \sim \Delta Y$

$$\vec{a}\cdot\Delta\vec{X} - \vec{A}\cdot\Delta\vec{X} \ll \vec{a}\cdot\Delta\vec{X} \sim \vec{A}\cdot\Delta\vec{X} \ .$$

Therefore, to avoid significant figure loss due to computer truncations to 8 significant figures in the calculation, $\vec{X}_0$ and $\vec{X}_1$ were picked such that

$$Z_0 = Z_1 = 0 \ . \qquad (11)$$

Results of repeated measurements showed the intersections to be reproducible within 5 cm for $\theta > 1°$ and within 8 cm for $\theta \sim .5°$ using the digitized scanner.

As a check on contamination from intersection errors, about 250 target empty frames at each energy were scanned and all good events

measured. Only one event was found with an intersection within the restricted hydrogen target. The measuring was about equally split between the manual and digitizing scanning machines.

2. THE PARAMETERS

Sources of systematic errors were the uncertainties in relative magnifications of the spark chamber views, and uncertainties in the coordinates of the centers of the spark chambers. For certain spark chamber views neither the edges nor the fiducial strips denoting the centers showed up clearly in any of the frames. A minimization technique using straight through tracks was used to correct for systematic errors in the parameters as follows.

Half a roll of film had been taken with the target empty and the anticoincidence circuit off. Of these 404 frames about 50 were selected that showed clear tracks and no apparent scattering. The data from these events were run through a computer program that varied the parameters and computed the average angle, $\bar{\theta}$, and separation distance, $\bar{D}$, between the tracks in the incoming and outgoing spark chambers for all the events. The final values of the parameters used were those where $\bar{\theta}$ and $\bar{D}$ were at minima, designated as $\bar{\theta}_{min}$ and $\bar{D}_{min}$, respectively.

For the manual scanning machine $\bar{\theta}_{min}$ was .11° and $\bar{D}_{min}$ was 1 mm. For the digitizing machine $\bar{\theta}_{min}$ was .07° and $\bar{D}_{min}$ was .75 mm. The standard deviations from zero were 10% larger than the above average values.

These values provided insight into the errors in measurement of events. Typical scattering events of about .5°, 1.5°, 2.5°, 4.5°, 6.5°, 7.5°, and 9.0° were each remeasured 25 times on the digitizing machine. The resulting distributions for $\overline{D}$ and $\overline{\theta}$ were plotted. In each case the entire distribution was contained within one standard deviation from zero of the straight through tracks.

At 2.01 and 3.15 BeV/c the data from the digitizing scanning machines were broken up in 1/2° bins. It was found that the average lab angle in each digitized bin was .2° smaller than that for the corresponding bin location for the manually scanned frames. Accordingly, the angular bins for 4.13 BeV/c and 4.95 BeV/c were shifted in by .2°.

For the digitized data the conditions on location of the event and the small angle limit (Chapter II-D) were relaxed to compensate for random losses from the manual scan. A 10% loss of events was found between the manual and digitizing scan. Careful examination of these lost events showed that most were marginal events from the manual scan.

D. Analysis of Scattering Events

A computer program analyzed the scanned data and reconstructed the events. The criteria for an elastic event were as follows:

1. The lab scattering angle had to be between the limits of the experimental setup

$$.5° < \theta < 10° .$$

2. The scatter occurred within the restricted hydrogen target, i.e., the scatter did not take place within 2 in. of either end of the hydrogen target. This requirement was made so that the gains and losses in events due to the intersection distribution were purely random.
3. The intersection distance was less than 3.5 mm. This requirement ruled out multiple elastic events.
4. The incoming pion was a beam particle. The incoming pion track was within the beam definition and its extension to the plane of the beam anti (beam anticoincidence counter) intersected the beam anti. This criterion ruled out skew particles which scattered within the hydrogen target.
5. Other restrictions were placed upon the event in order to fulfill solid angle requirements. For example, the scattered pion did not pass through the beam anti or the edge of the second downstream spark chamber.

Above all, the event had to be reproducible.

CHAPTER III

CORRECTIONS

A. Solid Angle

The range of azimuthal acceptance angles for scattered pions was restricted for $\theta_{lab} < 3.3°$ by the beam anti and for $\theta_{lab} > 2.7°$ by the downstream spark chambers, the other anticoincidence counters, and the mirror cutoff. In the overlap region the limitations on azimuth were independent of each other, so that corrections were additive.

The correction factors were calculated by a computer program which generated scatters from individual beam tracks at 17 equally spaced positions within the restricted hydrogen target. The computer program would determine the amount of azimuthal angle ϕ_{ijk} available for a scatter of angle θ_i from the j^{th} position in the target of the k^{th} beam track. The solid angle acceptance fraction $s(\theta_i)$ was just the average of the fraction over the beam and target.

$$s(\theta_i) = \sum_{k=1}^{n} \sum_{j=1}^{17} \frac{\phi_{ijk}}{2\pi} \frac{1}{17n} \quad . \tag{12}$$

Here n is the number of beam tracks used.

For $\theta_{lab} < 1.5°$ the correction factor was found to be very sensitive to the beam distribution and the location of the beam anticoincidence counter. As beam distribution data had been taken only at 4.95

BeV/c the incoming tracks for all good elastic events in the region $2.7° < \theta_{lab} < 3.3°$ were used as beam distributions for all four pion momenta. The beam anti, A_4, was located by plotting the intersection of tracks for all events with the plane of the counter.

For $\theta_{lab} > 2.7°$, the far downstream spark chamber was the biggest limiting factor on the solid angle. The other limitations of the mirror cutoff and the semi-cylindrical anti's were lumped together by projecting the anti's onto the downstream face of the first downstream spark chamber and requiring all elastic events to pass through this circle with a chord replacing an arc to compensate for the mirror cutoff. This condition was incorporated into the event reconstruction program.

The effective size of the second downstream spark chamber was cut down 1/4 in. on all sides to eliminate edge difficulties. This was also incorporated into the event reconstruction program.

The π^-p data were broken up into bins of π^- scattering angles, and solid angle acceptance fractions were computed in equal increments of t across each bin. The notation used was

$$S(t_i) = s(\theta_i) .$$

B. Scattering Angle Limits

1. SMALL ANGLE LIMIT

For laboratory scattering angles less than .5° event determination was unreliable. The statistics were poor for angles less than 1° due to the small azimuthal acceptance fraction. These two factors provided the basis for the small angle limit.

2. LARGE ANGLE LIMIT

The large angle limit was fixed by the requirement that the proton did not have sufficient energy to pass through the lead to trigger anti-coincidence counters C_{20} or C_{21}. From range-energy curves,[5] it was found that kinetic energies larger than 81 MeV were sufficient to reach the anticoincidence counters for a minimal path from a scattering point 1-1/2 in. from the beam axis. This corresponded to a t of -.154 $(\text{BeV/c})^2$.

The angular limits are summarized in Table I in terms of laboratory angles and t. At 2.01 BeV/c the pion could pass through the anti's for t less than -.106 $(\text{BeV/c})^2$.

C. Beam and Event Attenuation in the Target

As the incident beam moved through the target, particles were removed by interaction with the hydrogen so that fewer particles were available at the downstream end than at the upstream end. In addition

elastically scattered pions could undergo further scatters and these events would be lost by not satisfying the conditions from the computer program for good elastic events. At these small angles the path of the pion through the target from the point of scatter was, to a good approximation, the remainder of the length of the target. To this approximation, the resultant attenuation from these two effects can be totally expressed as an attenuation of the beam from one end to the other. The effective beam intensity, $\bar{N}_B$, is given in terms of the incident beam intensity, N, by

$$\bar{N}_B = Ne^{-L\rho\sigma} \tag{13}$$

where L is the total length (18 in.) of the target, σ is the π^-p total cross section for the given momentum, and ρ is the density of atoms/cc in liquid hydrogen. The effective beam fraction, ϵ_1, where

$$\epsilon_1 = \frac{\bar{N}_B}{N}$$

is given in Table II for the four momenta.

D. Beam Contamination

The primary contaminants of the beam were electrons and muons. All others were neglected.

The electron contamination was 2.2% at all momenta. This was taken directly from Damouth, et al.[1] and Ting's[3] estimates from the threshold

conditions of their Cherenkov counters. The electron contamination gives rise to an effective beam fraction ϵ_2 equaling .978.

The μ^- contamination was primarily due to the decay of the pion in flight and was estimated by direct calculations. Here as in Chapter III-C the incoming beam and the scattered pions were attenuated. Using a parallel argument the effective beam fraction, ϵ_3, is

$$\epsilon_3 = e^{-t/\gamma\tau} \tag{14}$$

where τ is the half life of the pion, $2.55 \cdot 10^{-8}$ sec, and

$$\gamma = E_{\pi\ lab}/m_\pi$$

$$t = L_1/\beta$$

$$\beta = p_{lab}/E_{\pi\ lab}$$

where $E_{\pi\ lab}$ and p_{lab} are respectively the laboratory energy and momentum of the pion, m_π is the pion mass, and L_1 is the distance from the downstream end of the H magnet to the last downstream spark chamber (593 cm).

Values of ϵ_2 and ϵ_3 are given in Table III.

The value of ϵ_2 was adjusted to account for the 30% of the π-μ decays where the μ's production angle brought them out of the beam at 2.01 BeV/c. No adjustment was needed at the other momenta.

E. Other Attenuations

Counter C_{11} also attenuated the beam in that the pion could have

scattered in this counter and still have been counted. This was not very likely to be the case for counters C_{10} and C_{12} due to their positions, and any of those which did make it through would have been subtracted as PS category (see Chapter II-A). For counter C_{11}

$$\epsilon_4 = e^{-L_2/L_o} = .994 , \qquad (15)$$

$$L_2 = .3175 , \qquad L_o = 52.3 \text{ cm} ,$$

where L_2 is the thickness of C_{11}, and L_o is the collision length in scintillator.[6]

Attenuations due to air, aluminum foil, and mylar were small. An estimate was that ϵ_5 covering these materials was .98.

The values for ϵ_4 and ϵ_5 are likewise in Table II.

F. Multiple Coulomb Scattering

Table III contains $\bar{\theta}_{lab}$ for multiple coulomb π^-p scattering in the hydrogen target. $\bar{\theta}_{lab}$ was found to be less than 1 milliradian at all four momenta so that no correction was necessary.

G. Momentum Resolution

The momentum resolutions are taken directly from Damouth, et al.[1] and Ting.[3] Table IV gives these values.

H. Correction of Apparent Elastic Events for Inelastic Interactions

1. π^-+p INELASTIC EVENTS

This experiment was not designed to see the path of the scattered proton or to measure the momentum of the scattered pion, so that there were no kinematic checks that could be made to rule out inelastic events from elastic events. The only means of ruling out inelastic events were through the anticoincidence counters and visual scanning which would show those inelastic events in which at least two charged particles came out at a small forward angle. Evidence will be given that inelastic events were not predominant and arguments will show inelastic contamination of the data was infact quite small. The exact amount of inelastic event contamination remains an uncertainty of this experiment.

a. Zero Prong Events (no charged particles in the final state)

Obviously no event contamination occurred from this type of reaction. However this channel offered a check on the conversion of gammas and subsequent detection of electrons in counters C_{20}, C_{21}, and C_{22}.

In general, zero prong reactions involved the production of a π° which quickly decayed into 2γ's, i.e.,

$$\pi^- + p \rightarrow n + m\pi^\circ \qquad m = 1,2,3, \ldots$$

$$\pi^\circ \rightarrow 2\gamma \ .$$

At 4.13 BeV/c a count of events in which tracks appeared in the

beam defining spark chambers but not in the downstream chambers gave a cross section of .5±.1 mb. The total cross section for zero prong events is 3.0±1 mb at 3.7 BeV/c.[7] Thus about 83% of the events were detected by the anticoincidence system. This compares favorably with the calculated 70% conversion in the lead of individual 200 MeV gammas into electron pairs.

b. Two Charged Particles in the Final State

The only competing two body final states were the reactions

$$\pi^- + p \rightarrow \Sigma^- + K^+$$

$$\pi^- + p \rightarrow \bar{P} + D \ .$$

Total production cross sections for these reactions have been found to be small, about 30 μb[8,9] within the general momentum range of this experiment, and so their contributions were negligible.

The other inelastics were of the forms

$$\pi^- + p \rightarrow \pi^- + p + m\pi^\circ, \qquad m = 1,2,3, \ \ldots$$

$$\pi^- + p \rightarrow \pi^- + \pi^+ + n + m\pi^\circ \ , \qquad m = 0,1,2, \ \ldots$$

Production cross sections for these processes have been found at 4.0 BeV/c to be about 5 mb and 9 mb,[10] respectively, so that their contributions could have been large.

c. Four or More Charged Particles in the Final State

Total cross sections for these productions were about 10 mb at 3.7 BeV/c. However, the probability of observing more than one charged particle in the downstream spark chambers and the probability of a charged particle having sufficient energy to pass through the lead and trigger the anticoincidence circuit was much larger than for the two charged particle final state.

To determine the extent to which channels b. and c. contributed to the contamination of the elastic scattering data, cross sections, σ_R, which were representative of the allowable elastic scatters for this experiment, were computed by integrating the nuclear term (Chapter IV-B, Eq. (8)) of the elastic differential cross section over the allowable range of t using reasonable values for the nuclear coefficients C and D.

Experimental cross sections, σ_E, which were representative of all the scatters involving two or more charged particles in the final state allowable for this experiment, were computed from the difference in target full and target empty event to beam ratios. The σ_E's were calculated to first order by

$$\left(1 - \left((E/B)_{FULL} - (E/B)_{EMPTY}\right)\right) = e^{-L\rho\sigma} \qquad (16)$$

$$\sigma_E = \sigma - \sigma_{\text{observed zero prongs}}.$$

Table V contains the values of σ_R and σ_E for the four laboratory momenta. The average agreement between σ_R and σ_E is within 22%. Therefore, the background could not have been predominant.

Table X contains a comparison of the nuclear coefficient, C, determined from this experiment, other experiments, and from theory using the optical theorem and dispersion relations. The best value from this experiment and the values predicted by theory agree on the average to within 5%.

In the differential cross section range where these data overlap with Damouth, et al.[1] and Perl, et al.[2] the agreement is good (Figs. 10-13). Since it is expected that the differential cross sections for inelastic processes have negligible dependence on θ for small θ, the overlap range should have the largest percentage of inelastic contamination. On this basis calculations of inelastic contamination were made from the counting rates of a bubble chamber experiment at 4.0 BeV/c.[10] The results give an upper bound to the inelastic contamination to the elastic differential cross section of .36 mb/sr. The corresponding partial cross section for these inelastics at this momentum is about 2.5% of σ_R.

2. OTHER REACTIONS

a. π-μ Decay

For 2.01 BeV/c the maximum laboratory decay angle between π^- and μ^-

was 1.123°. A decay in the target could look like an elastic scatter and so a subtraction was necessary. The laboratory distribution was calculated from the isotropic center-of-mass π-μ decay distribution. The laboratory distribution was then folded in with the solid angle acceptance fractions and this new distribution was broken up into angular bins and subtracted from the corresponding π^--p experimental data bins.

For the other momenta the maximum lab angles of the μ^- were less than the minimum angles of the data and so no correction was needed.

b. $\mu^- + p$, $e^- + p$

The reactions are all coulomb reactions. Differential cross sections for these coulomb reactions are less than 1 μb/sr for the angular range considered and so their contributions were negligible.

CHAPTER IV

ELASTIC SCATTERING RESULTS

A. The Data

The elastic scattering data were broken up into angular bins corresponding roughly to 1/2° in the laboratory. Center-of-mass differential cross sections, $\Delta\sigma/\Delta\Omega$, were calculated by the following formula:

$$\left(\frac{\Delta\sigma}{\Delta\Omega}\right)_i = \frac{n_i}{NL\rho 2\pi(\Delta \cos \theta^*)_i} \cdot \frac{1}{\epsilon} \qquad (17)$$

where

n_i = total number of events in the i^{th} bin

N = total number of incoming pions (calculated from Eq. (1))

L = restricted target length = 14.18 in.

ρ = density of liquid hydrogen in protons per cubic centimeter = 4.196×10^{22}

$(\Delta \cos \theta^*)_i$ = difference in cosines of the center-of-mass angles corresponding to the end points of the i^{th} bin

ϵ = normalization corrections = $\epsilon_1 \cdot \epsilon_2 \cdot \epsilon_3 \cdot \epsilon_4 \cdot \epsilon_5$ (from Table II).

For 2.01 BeV/c, n_i in Eq. (1) was replaced by $n_i - n_\mu$ where n_μ, was the

number of events attributed to $\pi^-\mu$ decays.

Since Eq. (1) did not contain a correction for solid angle, $\Delta\sigma/\Delta\Omega)_i$ was the center-of-mass elastic differential cross section as seen by this experiment. The method of finding the corrected differential cross section, $d\sigma/d\Omega)_i$, is explained in Chapter IV-B.

At 3.15 BeV/c using 1/2° bins the curve fit (see Chapter IV-B) gave a negative value to the pure Coulomb term, i.e., $A < 0$. Therefore the data were redivided into 1/4° bins.

B. The Curve Fit

1. INTERFERENCE MODEL

The small angle π^-+p elastic differential cross section in the center of mass can be approximated by the simple interference model[11,12]

$$\frac{d\sigma(t)}{d\Omega} = \frac{A}{t^2} - \frac{B}{t} + Ce^{Dt} \qquad (18)$$

where A/t^2 is a pure Coulomb contribution, $-B/t$ is the interference contribution, and Ce^{Dt} is the nuclear diffraction peak contribution.

The Coulomb amplitude is real and equal to $(-\sqrt{A}/t)$. The nuclear amplitude is (D_-+iE) so that

$$\frac{d\sigma}{d\Omega} = \left(\frac{-\sqrt{A}}{t} + D_-\right)^2 + E^2 = \frac{A}{t^2} - \frac{2\sqrt{A}D_-}{t} + (D_-^2+E^2) \qquad (19)$$

by comparison with Eq. (18), assuming D_- is slowly varying for smaller $|t|$,

$$D_- \simeq \frac{B}{2\sqrt{A}} \tag{20}$$

$$(D_-^2+E^2) \simeq Ce^{Dt} \tag{21}$$

now $t < 0$ so that if $B < 0$ then $D_- < 0$ and the interference is destructive.

2. FOLDED FIT

The solid angle acceptance fraction varied rapidly within many of the angular bins so that using average acceptance fraction values introduced spurious errors. Therefore, to fit the data the solid angle acceptance fraction was folded into Eq. (17)

$$\frac{1}{\Delta t_i}\int_{t_i-\Delta t_i/2}^{t_i+\Delta t_i/2}\frac{d\sigma}{d\Omega}(t)S(t)dt = \frac{1}{\Delta t_i}\int_{t_i-\Delta t_i/2}^{t_i+\Delta t_i/2} dt\, S(t)\left(\frac{A}{t^2}+\frac{B}{t}+Ce^{dt}\right) \tag{22}$$

Here t_i is the average t for the i^{th} bin of width Δt_i. The left hand side of Eq. (22) is just $\Delta\sigma/\Delta\Omega\,(t_i)$, the differential cross section uncorrected for solid angle. Rewriting Eq. (22)

$$\frac{\Delta\sigma}{\Delta\Omega}(t_i) = \frac{1}{\Delta t_i}\int_{t_i-\Delta t_i/2}^{t_i+\Delta t_i/2}\frac{d\sigma}{d\Omega}(t)S(t)dt \tag{23}$$

$$\frac{\Delta\sigma(t_i)}{\Delta\Omega} = \left[\frac{1}{\Delta t_i}\int_{t_i-\Delta t_i/2}^{t_i+\Delta t_i/2}\frac{S(t)dt}{t^2}\right]A - \left[\frac{1}{\Delta t_i}\int_{t_i-\Delta t_i/2}^{t_i+\Delta t_i/2}\frac{S(t)dt}{t}\right]B + \left[\frac{1}{\Delta t_i}\int_{t_i-\Delta t_i/2}^{t_i+\Delta t_i/2}S(t)e^{Dt}dt\right]C \quad . \tag{24}$$

The coefficients of A, B, and C were evaluated by a trapezoidal numerical integration using steps of $(\Delta t_i/5)$ or smaller.

A weighted least squares program was used to find A, B, C, and D by minimizing the quantity

$$\sum_i \left[\left(\frac{\Delta\sigma(t_i)}{\Delta\Omega} - \frac{\Delta\sigma}{\Delta\Omega}\right)_i\right)^2 \Bigg/ \left(\frac{\Delta\sigma}{\Delta\Omega}\right)_i\Bigg)^2\Bigg] f(i)$$

and iterating in D. Here f(i) was the weighting factor, which in general was the number of events observed in the t_i bin, and $\Delta\sigma/\Delta\Omega)_i$ was calculated from Eq. (17).

As an exception the 4.95 BeV/c data were fit to the curve

$$\frac{d\sigma}{d\Omega} = Ce^{Dt} \qquad (25)$$

using a similar procedure because the data did not extend into the Coulomb region.

3. SOLID ANGLE CORRECTION FACTOR

To find the solid angle correction factor for $\Delta\sigma/\Delta\Omega)_i$, the following method was used:

a. Equation (23) was evaluated to give $\Delta\sigma/\Delta\Omega\ (t_i)$.

b. Applying the mean value theorem to the integral in Eq. (23)

$$\frac{\Delta\sigma(t_i)}{\Delta\Omega} = \frac{1}{\Delta t_i} \cdot \frac{d\sigma(t')}{d\Omega} S(t') \cdot \Delta t_i = \frac{d\sigma(t')}{d\Omega} S(t') \qquad (26)$$

$$|t'-t_i| \leq \Delta t_i/2 \ .$$

c. From $\frac{d\sigma}{d\Omega}(t)$, S(t), and $\frac{\Delta\sigma}{\Delta\Omega}(t_i)$ Eq. (26) was solved for S(t') and $\frac{\Delta\sigma}{\Delta\Omega}(t')$.

d. S(t') was used as the correction factor for $\Delta\sigma/\Delta\Omega)_i$, i.e.,

$$\frac{d\sigma}{dt}\Big)_i = \frac{1}{S(t')} \cdot \frac{\Delta\sigma}{\Delta\Omega}\Big)_i .$$

e. In case of multi-valued solutions, the average of the S(t') was used. For graphing purposes $d\sigma/d\Omega)_i$ was plotted at the middle of the bin.

C. Results

The results for the nuclear diffraction peak term are in good agreement with Damouth, et al.[1] and Perl, et al.[2,13] in the nuclear diffraction peak term. The best values of the real part of the nuclear scattering amplitudes are consistent with the theoretical predictions for $D_- < 0$.

The results are presented as follows:

1. Tables VI-IX contain the π^-+p elastic differential cross sections and other pertinent information for 2.01, 3.15, 4.13, and 4.95 BeV/c, respectively. At 2.01 BeV/c the elastic events for $|t|$ of .0008 and .0021 $(BeV/c)^2$ have been corrected for π^--μ^- decays (no. of $\pi\mu$'s are in parentheses).
2. Table X shows the values of the coefficients A, B, C, and D, found from this experiment, compared with results from

Damouth, et al.[1] and Perl, et al.,[2] and from theory. D_- for this experiment was calculated from Eq. (20).

3. Table XI contains the Pearson $P(\chi^2)$ values for the fitted curves. For 3.15 BeV/c the 1/4° bin fit gave a $P(\chi^2)$ of about .8 while the 1/2° fit was .95, justifying the use of the 1/4° bin fit. For 2.01 BeV/c both 1/4° and 1/2° bin fits gave $P(\chi^2) < .01$. The 1/2° bin fit, however, had the larger $P(\chi^2)$ and is the one presented. The two fits gave consistent results. For 4.13 and 4.95 BeV/c only 1/2° bin fits were made.

4. Figures 6-9 show the differential cross sections for this experiment for the four momenta 2.01-4.95 BeV/c, respectively. The simple interference fit and the nuclear term from this fit are plotted. The 4.95 BeV/c data were only fit to the nuclear diffraction peak curve.

5. Figures 10-13 are composite results of this experiment, Damouth's[1] experiment, and Ting's[2] experiment. Figure 13 compares the nuclear fit from this experiment with that of Ting's at 4.95 BeV/c.

CHAPTER V

FORMAL DERIVATION OF DISPERSION RELATIONS FOR FORWARD $\pi^{\pm}p$ ELASTIC SCATTERING AMPLITUDE

A dispersion relation is a homomorphism whereby the real part of a function of a complex variable $f(z)$ is expressed as a function of the imaginary part of $f(z)$

$$\mathrm{Re}f(z) = G(\mathrm{Im}\, f(z), z) \ . \tag{27}$$

Knowing Im $f(z)$, Eq. (27) then becomes a means for finding Re$f(z)$. The purpose of this chapter is to find this equation for the case of the forward $\pi^{\pm}p$ elastic scattering amplitude. In this case the optical theorem gives the form of Im $f(z)$.

Such an equation for forward $\pi^{\pm}p$ elastic scattering can be derived from contour integration. By this procedure the problem can be redefined as follows:

1. To find the analytic properties of the analytic continuation of some function of the scattering amplitude into the complex plane for all its variables.
2. To perform the integration inserting appropriate boundary conditions.

The Mandelstam approach is used to formally derive the dispersion relations. The units used in the derivation are such that

$$\hbar c = 1$$

so that distances are measured in units of $(\text{energy})^{-1}$.

A. Kinematics

The purpose of this section is to define convenient variables to handle the scattering problem. Consider the interaction in Fig. 14. p_1, p_2, p_3, and p_4 are four momenta.

New kinematic variables, s, t, and u, are introduced to describe this sytem.

$$\begin{aligned} s &= (p_1+p_2)^2 \\ t &= (p_1-p_3)^2 \\ u &= (p_1-p_4)^2 \ . \end{aligned} \tag{28}$$

By the conservation laws there are only two independent kinematic variables and hence the constraint equation

$$s + t + u = 2m^2 + 2\mu^2 \tag{29}$$

$$m = \text{mass of proton}$$

$$\mu = m_\pi \ .$$

From this point on all considerations are made in the center-of-mass system unless otherwise stated. Using channel I as reference (Fig. 14), time is oriented such that the reaction is

$$\pi^- + p \rightarrow \pi^- + p \ .$$

The variable s is just the square of the center-of-mass energy, called the energy variable, and t is just the square of the four momentum transfer.

For channel II the reaction is

$$p + \bar{p} \rightarrow \pi^- + \pi^+$$

and t is the energy variable.

For channel III the reaction is

$$\pi^+ + p \rightarrow \pi^+ + p$$

and u is the energy variable. t is the square of the four momentum transfer. The variables for channels I and III display the following exchange of roles:

I		III
s	$\longleftrightarrow$	u
t	$\longleftrightarrow$	t
u	$\longleftrightarrow$	s .

This will be convenient in deriving the dispersion relations.

Channel I is also called the s channel; II the t channel; III the u channel.

A composite picture of the physical regions for the three channels can be drawn in two dimensions (see Fig. 15). Three axis s, t, and u are orientated mutually 120° out of phase with units appropriate to satisfy the constraint Eq. (29). The boundaries for the physical region for each channel are found by the physical conditions

$$\text{energy variable} \geq (\Sigma(\text{of incoming masses}))^2$$

$$-1 \leq \cos\theta \text{ c.m.} \leq +1.$$

The physical regions are shown in Fig. 15 as the ruled areas.

B. Mandelstam Hypothesis and the Invariant Amplitude

1. SINGULARITIES

The ordinary scattering amplitude is not relativistically invariant. A dispersion relation can most easily be derived for the invariant amplitude $A(s,t,u)$ which is studied in this section.

Consider the reaction

$$A + B \rightarrow C + D \qquad (s, \text{ the energy variable})$$

The Mandelstam hypothesis[14] states that for each energy threshold, s_o, allowing a new channel of interaction, $A(s,t,u)$ has a singularity in the energy variable. These singularities are simple poles for bound states since the reaction can only occur for $s = s_o$. For all other channels the singularities are branch points. The reaction can occur for $s_o \leq s \leq \infty$ and hence there is a line of singularities. There can be no complex singularities from this hypothesis, for threshold energies are real. All reactions must satisfy appropriate conservation laws such as spin, parity, etc.

Applying this to the reaction

$$\pi^- + p \rightarrow \pi^- + p,$$

there is an unphysical pole in A(s,t,u) at

$$s = m^2 \qquad \text{(see Fig. 16)}$$

corresponding to a neutron bound state and in the physical region an elastic cut for

$$(m + \mu)^2 \leq s \leq \infty .$$

There are further cuts for inelastic processes but all are contained in the elastic cut. The sum total of all the cuts is called the right hand cut.

For the u channel the reaction is

$$\pi^+ + p \rightarrow \pi^+ + p .$$

There is a corresponding unphysical neutron pole in A(s,t,u) at

$$u = m^2 \qquad \text{(called the crossed pole—see Fig. 17)}$$

and the left hand cut

$$(m + \mu)^2 \leq u \leq \infty .$$

For fixed t all the singularities of the s and u channel can be plotted in the complex s plane by making use of the constraint Eq. (29). Figure 18 is such a plot for fixed small negative t. $t < 0$ is just a physical condition for both s and u channels.

2. CROSSING SYMMETRY

Crossing symmetry provides a means of relating $A_I(s,t,u)$ and $A_{III}(s,t,u)$ (I and III denote the channels). For simplicity the crossing symmetry will be found for spin zero particles for the reaction

$$A + B \rightarrow C + D$$

$$\overline{B} = D$$

$$\overline{D} = B \ .$$

The reactions in the s and u channels are identical. By this symmetry and by the exchange roles of s and u found in Chapter V-A it is postulated that

$$A_{III}(u,t,s) = A_I(s,t,u) \ ,$$

so that unphysical values of III can be found from physical values of I and vice versa, and A_I and A_{III} are analytic continuations of each other.

For pion-proton elastic scattering the formulation is more difficult in that there are four invariant amplitudes. This is so because the reactions are spin and isotopic spin dependent.

Formally, the crossing symmetry can be written for fixed negative t as[15]

$$T^{(\pm)}(u,t,s) = \pm T^{(\pm)}(s,t,u) \qquad (30)$$

where

$$T^{(\pm)} = (1/2)(T_- \pm T_+) \tag{31}$$

$$T_+ = T^{(3/2)}$$

$$T_- = (2/3)T^{(3/2)} + (1/3)T^{(1/2)}$$

where the T's are invariant amplitude, the superscripts 3/2 and 1/2 denote total isotopic spin, and the subscripts, + and -, correspond to the reactions

$$\pi^{\pm} + p \rightarrow \pi^{\pm} + p \ .$$

The amplitudes $T^{(\pm)}$ each have the same singularities as shown in Fig. 18 as they are linear combinations of A_I and A_{III}.

The crossing symmetry can be simplified through a change of variables. s evaluated in the laboratory system is

$$s = m^2 + \mu^2 + 2m\nu - 1/2\ t \tag{32}$$

$$\nu = \omega + t/(4m) \tag{33}$$

where ω is the total energy of the incident pion in the laboratory system. Solving Eqs. (29) and (32) for u,

$$u = m^2 + \mu^2 - 2m\nu - 1/2\ t \ . \tag{34}$$

Substituting the values for s and u from Eqs. (32) and (34), respectively, into Eq. (30), the crossing symmetry becomes

$$T^{(\pm)}(-\nu,t) = \pm T^{(\pm)}(\nu,t) \tag{35}$$

where the convention was used

$$T^{(\pm)}(s(\nu,t),t,u(\nu,t)) \rightarrow T^{(\pm)}(\nu,t) \ .$$

Plotted in the complex ν plane, the singularities lie on the Re ν axis and are symmetric to the Im ν axis. This is shown in Fig. 19.

C. Complex Integration

A Cauchy integral can now be set up for $T^{(\pm)}(\nu,t)$.

$$T^{(\pm)}(\nu_o,t) = \frac{1}{2\pi i} \oint_C \frac{T^{(\pm)}(\nu',t)}{\nu'-\nu_o} \, d\nu' \tag{36}$$

where the path of integration is shown in Fig. 19.

Evaluation of the integral in Eq. (36) along the infinite semicircles C_1 and C_2 will give zero if $T^{(\pm)}/\nu \rightarrow 0$ as $\nu \rightarrow \infty$. From Pomeranchuk's Theorem[15] this may hold for $T^{(-)}$ but is not so likely to be the case for $T^{(+)}$. An integral which is more likely to converge for $T^{(+)}$ is

$$T^{(+)}(\nu_o,t) = \frac{(\nu_o-(\mu+t/4m))}{2\pi i} \oint_C \frac{T^{(+)}(\nu',t)\,d\nu'}{(\nu'-(\mu+t/4m))(\nu'-\nu_o)} \ . \tag{37}$$

The remainder of this derivation will be concerned with the dispersion relation for $T^{(-)}$ with results quoted for $T^{(+)}$ at the end of the chapter.

From Eq. (36), evaluated along C,

$$T^{(-)}(\nu_o,t) = \frac{1}{2\pi i}\left[\int_{\mu+t/4m}^{\infty} + \int_{-\infty}^{-\mu-t/4m}\right]\cdot\left[\frac{T^{(-)}(\nu'+i\epsilon,t)-T^{(-)}(\nu'-i\epsilon,t)}{\nu'-\nu_o}\right]d\nu' \tag{38}$$

$$+ \text{ pole terms.}$$

From potential scattering and also evaluation of Feynman diagrams $T^{(\pm)}$ are found to be real in the unphysical region ($|\nu| < \mu+t/4m$) along the Re ν axis. Thus the Schwartz Reflection Theorem gives

$$T^{(\pm)}(\bar{\nu},t) = \overline{T^{(\pm)}(\nu,t)}. \tag{39}$$

As $\epsilon \to 0$, the numerator in the integrand in Eq. (38) becomes

$$\lim_{\epsilon\to 0}(T^{(-)}(\nu'+i\epsilon,t) - T^{(-)}(\nu'-i\epsilon,t)) = \text{Im } T^{(-)}(\nu',t)2i \tag{40}$$

which means that the discontinuity in $T^{(-)}$ on the real axis is in the imaginary part.

From Eqs. (35), (38) and (39)

$$T^{(-)}(\nu_o,t) = \frac{1}{\pi}\int_{\mu+t/4m}^{\infty} \text{Im } T^{(-)}(\nu',t)\left[\frac{1}{\nu'-\nu_o} + \frac{1}{\nu'+\nu_o}\right]d\nu'$$

$$+ \text{ pole terms.} \tag{41}$$

Now setting

$$\nu_o = \nu + i\epsilon \tag{42}$$

where ν is real and taking the real part of Eq. (41)

$$\text{Re } T^{(-)}(\nu,t) = \frac{1}{\pi}\int_{\mu+t/4m}^{\infty} \text{Im } T^{(-)}(\nu',t)\left[\frac{(\nu'-\nu)}{(\nu'-\nu)^2+\epsilon^2}+\frac{(\nu'+\nu)}{(\nu'+\nu)^2+\epsilon^2}\right]$$

$$+ \text{ pole terms.} \tag{43}$$

Letting ϵ and $t \to 0$ and using Eq. (33)

$$\text{Re } T^{(-)}(\omega,o) = \frac{2\omega}{\pi} P\int_{\mu}^{\infty} \frac{\text{Im } T^{(-)}(\omega',o)}{\omega'^2-\omega^2}\, d\omega' + \text{pole terms} \tag{44}$$

where P stands for the principal part.

The pole terms can be evaluated from Feynman diagrams and yield

$$\text{pole terms} = \frac{G_r^2\omega}{2m}\left(\frac{1}{\omega-\mu^2/2m}-\frac{1}{\omega+\mu^2/2m}\right) = \frac{f^2 8\pi\omega}{\omega^2-(\mu^2/2m)^2} \tag{45}$$

where G_r^2 is the rationalized renormalized pseudoscalar coupling constant. The pole terms are written in the form of the right hand side of Eq. (45) to conform with the literature. From Eqs. (44) and (45)

$$\text{Re } T^{(-)}(\omega,o) = \frac{8\pi f^2\omega}{\omega^2-(\mu^2/2m)^2} + \frac{2\omega}{\pi} P\int_{\mu}^{\infty} \frac{\text{Im } T^{(-)}(\omega',o)\,d\omega'}{\omega'^2-\omega^2}\,. \tag{46}$$

The above equation is an invariant amplitude dispersion relation.

D. Transformation to the Scattering Amplitude Dispersion Relations

Evaluating the invariant amplitude in the center of mass,

$$T^{(-)}(\omega,o) = f_{cm}^{(-)}(\omega)\,.\,E_{cm}/(4\pi m) \tag{47}$$

where $f^{(-)}_{cm}(\omega)$ is just the center-of-mass forward scattering amplitude. Now

$$\frac{f^{(-)}_{cm}}{p_{cm}} = \frac{f^{(-)}_{lab}}{p_{lab}} \tag{48}$$

where p_{cm} and p_{lab} are the center-of-mass and lab momentum of the pion, respectively, and $f^{(-)}_{lab}(\omega)$ is the laboratory forward scattering amplitude.

$$T^{(-)}_{(\omega,o)} = \frac{f^{(-)}_{lab}(\omega)}{4\pi} . \tag{49}$$

The real part of $f^{(-)}_{lab}(\omega)$ is written as

$$\text{Re } f^{(-)}_{lab}(\omega) = D^{(-)}(\omega) \tag{50}$$

and by the optical theorem

$$\text{Im } f^{(-)}_{lab}(\omega) = \frac{k\sigma^{(-)}(\omega)}{4\pi} \tag{51}$$

where k is the lab momentum of the incoming π and

$$\sigma^{(-)}(\omega) = 1/2\ (\sigma_-(\omega) - \sigma_+(\omega)) . \tag{52}$$

Using Eqs. (49), (50), and (51), Eq. (46) becomes the conventional unsubtracted dispersion relation

$$D^{(-)}(\omega) = \frac{2f^2\omega}{\omega^2-(\mu^2/2m)^2} + \frac{\omega}{2\pi^2} P\int_{\mu}^{\infty} \frac{k\sigma^{(-)}(\omega')}{\omega'^2-\omega^2}\, d\omega' \tag{53}$$

where

$$D^{(-)} = 1/2\ (D_- - D_+) \tag{54}$$

and $D_\pm$ are the real parts of the lab elastic forward scattering amplitude for $\pi^\pm + p$.

Evaluating the integral in Eq. (37), using the same procedure as for $T^{(-)}$, the result is a subtracted dispersion relation

$$D^{(+)}(\omega) = \frac{f^2 k^2 \mu^2}{m(\mu^2-(\mu^2/2m)^2)(\omega^2-(\mu^2/2m)^2)} + D^{(+)}(\mu)$$

$$+ \frac{k^2}{2\pi^2} P \int d\omega' \frac{\omega'}{k'} \frac{\sigma^{(+)}(\omega')}{\omega'^2-\omega^2} \tag{55}$$

where

$$D^{(+)} = 1/2\ (D_- + D_+) \tag{56}$$

and

$$\sigma^{(+)} = 1/2\ (\sigma_- + \sigma_+)\,. \tag{57}$$

Substituting $T^{(-)}$ for $T^{(+)}$ in Eq. (37), another subtracted dispersion relation is found

$$D^{(-)}(\omega) = \frac{\omega}{\mu} D^{(-)}(\mu) + \frac{2f^2}{1} \frac{\omega k^2}{(\mu^2-(\mu^2/2m)^2)(\omega^2-(\mu^2/2m)^2)}$$

$$+ \frac{\omega k^2}{2\pi^2} P \int_\mu^\infty \frac{d\omega'}{k'} \frac{\sigma^{(-)}(\omega')}{\omega'^2-\omega^2}\,. \tag{58}$$

An additional equation relating the constants $D^{(-)}(\mu)$ and f^2 is found by evaluating Eq. (53) for $\omega = \mu$.

$$D^{(-)}(\mu) = \frac{2f^2\mu}{\mu^2-(\mu^2/2m)^2} + \frac{\mu}{4\pi^2}\int_{\mu}^{\infty} d\omega' \frac{\sigma^{(-)}(\omega')}{k'} . \qquad (59)$$

Taking the sum and difference of Eqs. (55) and (58) gives the conventional form of the subtracted dispersion relations for forward $\pi^{\pm}$+p elastic scattering.

$$D_{\pm}(\omega) = \frac{1}{2}(1 \mp \omega/\mu) D_{-}(\mu) + \frac{1}{2}(1 \pm \omega/\mu) D_{+}(\mu)$$

$$+ \frac{2f^2k^2}{(-(\mu^2/2m) \pm \omega)(\mu^2-(\mu^2/2m)^2)}$$

$$+ \frac{k^2}{4\pi^2} P\int_{\mu}^{\infty} \frac{d\omega'}{k'} \left[\frac{\sigma_{\pm}(\omega')}{\omega'-\omega} + \frac{\sigma_{\mp}(\omega')}{\omega'+\omega} \right] \qquad (60)$$

CHAPTER VI

DISPERSION CALCULATIONS

A. Method of Evaluation of $D_{\pm}$

Equation (60) was evaluated as follows:

1. THE INTEGRALS

Each integral was broken up into a sum of sub-integrals whose limits of integration were such that $\sigma_{\pm}(\omega)$ could be approximated as linear in ω over the range of integration. Each sub-integral was then evaluated explicitly. Thus the sum of sub-integrals became a sum of end point contributions.

The upper limit of integrations, ω_i, for the i^{th} sub-integral was such that

a. $\omega_i < 3$ BeV

$\Delta\omega_i = \omega_i - \omega_{i-1} = 10$ MeV

b. 3 BeV $< \omega_i <$ 10 BeV

$\Delta\omega_i = 500$ MeV

c. 10 BeV $< \omega_i <$ 30 BeV

$\Delta\omega_i = 2$ BeV .

Above 30 BeV the integration was also done explicitly by assuming a constant cross section.

This method of integration was used originally in the dispersion calculations of Cronin.[16]

2. THE CROSS SECTIONS

Figure 20 is a plot of the total cross sections used as a function of pion laboratory kinetic energy, T, for 10 MeV < T < 10 BeV. The σ_+ peak at T of about 175 MeV, not completely depicted in the graph, has a maximum of 200 mb. The cross sections were taken from the following experiments:

a. $0 \leq T < .3$—a composite of experimental results.[17]

b. $.3 < T \lesssim .7$ BeV—Bareyre, et al.[18]

c. $.5 \lesssim T \leq 1.6$ BeV--Devlin, et al.[19]

d. $1.6 < T \leq 4.2$ BeV—Diddins, et al.[20]

e. $4.2 < T \leq 20.0$ BeV—Von Dardel, et al.[21]

f. $20.0 \leq T \leq 30.0$ BeV—extrapolation from Von Dardel's[21] results and tapered to assumed asymptotic limits of 24.51 and 23.80 mb for σ_- and σ_+, respectively, at 30 BeV.

For a. all of the data with error bars were plotted on a large graph and then a visual curve fit was made. The points to be used were read off of this fit. For $T > .3$, the points were read off the published fitted curves with smooth extrapolations made in overlap regions.

3. THE PARAMETERS

The parameters for Eqs. (53) and (60) as determined by Woolcock[15,22] are

$$f^2 = .081 \pm .002$$

$$a_1 = .171 \pm .005$$

$$a_3 = -.088 \pm .004$$

$$D^{(+)}(\mu) = \frac{m+\mu}{m\mu} \cdot \frac{1}{3}(a_1+2a_3) = (-.014 \pm .025)/\text{BeV}$$

$$D^{(-)}(\mu) = \frac{m+\mu}{m\mu} \cdot \frac{1}{3}(a_1-a_3) = (.711 \pm .018)/\text{BeV}.$$

Direct evaluation of Eq. (59) truncating the integration at 30 BeV gave

$$D^{(-)}(\mu) = .733/\text{BeV} \tag{61}$$

in agreement with the value above.

The values of the parameters used for the calculations were Woolcock's values for f^2 and $D^{(+)}(\mu)$, and $D^{(-)}(\mu)$ from Eq. (61). $D_+(\mu)$ and $D_-(\mu)$ were calculated using Eqs. (54) and (56).

B. The Results

The results were calculated on an IBM 7090 computer and are presented as follows:

1. Table XII contains the calculated values of D_+, D_-, and $D^{(-)}$ in the center of mass for 1 BeV < T < 30 BeV. The values of $D^{(-)}$ were calculated from $D_\pm$ using Eq. (54). An estimate of errors is about ±10% for $D_\pm$ based upon normalization uncertainties in the cross sections, and the uncertainties in the extrapolation of $\sigma_\pm$ to their assumed asymptotic values. Uncertainties in $D^{(-)}$ are much larger since

$\sigma^{(-)}$ is proportional to the difference of σ_+ and σ_-.

2. Table XIII contains the ratios of the real to the imaginary part of the forward scattering amplitudes determined from this experiment and from the dispersion calculations.

3. Figure 21 is a plot of the ratio of the real to the imaginary part of the forward scattering amplitude as calculated from dispersion relations. The crossover of the π^+ and π^- curves at 19 BeV may be due to the choice of asymptotic limits for $\sigma_\pm$. The best values of the points determined from this experiment are also plotted. The ratios are denoted as $D_\pm/\mathrm{Im}f_\pm$ where $f_\pm$ stand for the center-of-mass forward elastic scattering amplitudes for $\pi^\pm$+p, respectively, and $\mathrm{Im}f_\pm$ are defined by the optical theorem in a similar manner to Eq. (50), replacing $\sigma^{(-)}(\omega)$ by $\sigma_\pm(\omega)$ and k by the center-of-mass momentum of the incoming π.

CHAPTER VII

CONCLUSION

The following results have been presented here pertaining to high energy elastic π^-+p scattering:

1. The experimental method of using spark chambers to observe the pion and eliminating inelastic background through anticoincidence circuitry without observing the proton has been found to be valid for selecting small angle elastic scatters at these energies. The differential cross sections found obeyed an exponential law as has previously been seen at larger momentum transfers. A departure from this exponential law was seen at very small momentum transfers where the Coulomb contribution became significant. On this basis direct calculations of the real part of the forward scattering amplitude were made using a simple interference model.

2. The best experimental values found for the real part of the forward scattering amplitude are consistent with dispersion theory predictions that $D_- < 0$. The classical analog to this is that a repulsive potential is involved in the interaction.

3. Dispersion calculations were carried to higher energies using recent $\pi^{\pm}$+p total cross sections. $D_{\pm}$ were found to give sizable contributions to the forward scattering amplitude above 1 BeV. D_+ reached a peak of almost 50% of the value of the imaginary part of the

amplitude at 1.6 BeV/c. At 20 BeV the contributions of $D_{\pm}$ were still about 10%. These amounted to only about 1% contributions to the differential cross sections in the diffraction region since the contributions go as the square of the amplitudes. However in the region of significant Coulomb scattering, the interference would still be sizable.

VIII. BIBLIOGRAPHY

1. D. E. Damouth, L. W. Jones, and M. L. Perl, University of Michigan Technical Report No. 03106-11-T (1963).

2. M. L. Perl, L. W. Jones, and C. C. Ting, Phys. Rev. 132, 1252 (1963).

3. C. C. Ting, Doctoral thesis, University of Michigan, unpublished, 1963.

4. D. I. Meyer and K. M. Terwilliger, Rev. of Sci. Inst. 32, 512 (1961).

5. J. Atkinson, Jr., and B. Willis, UCRL-2426, Vol. II (1957).

6. W. H. Barkas and A. H. Rosenfeld, UCRL-8030 Rev., (1963).

7. Y. Y. Lee, University of Michigan Technical Report No. 04938-1-T (1964).

8. F. S. Crawford, et al., Phys. Rev. Letters 3, 394 (1959).

9. M. L. Perl, L. W. Jones, and C. C. Ting, Phys. Rev. 132, 1273 (1963).

10. L. Bondar, K. Congartz, M. Deutschmann, et al., Nuovo Cimento 31, 729 (1964).

11. R.J.N. Phillips, Physics Letters 3, 184 (1963).

12. S. J. Lindenbaum, Preprint of Talk Given at the Int. Conf. of High Energy Physics, DUBNA (1964).

13. M. L. Perl, L. W. Jones, and C. C. Ting, University of Michigan Technical Report No. 03106-10-T (1963).

14. R. Omnes and M. Froissart, Mandelstam Theory and Regge Poles, p.80, W. A. Benjamin, Inc. (1963).

15. J. Hamilton and W. S. Woolcock, Rev. Mod. Phys. 35, 737 (1963).

16. J. W. Cronin, Phys. Rev. 118, 824 (1960).

17. V. S. Barashenkov, V. M. Maltsen, Fortschritte der Physik 9, 549 (1961).

18. P. Bareyre, et al., Physics Letters 8, 173 (1964).

19. T. J. Devlin, et al., Phys. Rev. 125, 690 (1962).

20. A. N. Diddens, et al., Phys. Rev. Letters 10, 262 (1963).

21. G. von Dardel, et al., Phys. Rev. Letters 8, 173 (1962).

22. J. Hamilton and W. S. Woolcock, Phys. Rev. 118, 291 (1960).

TABLE I

LIMITS OF RANGE OF EXPERIMENT

	2.01 BeV/c	3.15 BeV/c	4.13 BeV/c	4.95 BeV/c
Small laboratory angle limit	.497°	1.009°	1.156°	1.065°
$\|t\|_{minimum}$	.0003 $(BeV/c)^2$	.0031 $(BeV/c)^2$	.0069 $(BeV/c)^2$	.0085 $(BeV/c)^2$
Large laboratory angle limit	9.44°	7.23°	5.48°	4.49°
$\|t\|_{maximum}$	.106 $(BeV/c)^2$	.154 $(BeV/c)^2$	.153 $(BeV/c)^2$	.148 $(BeV/c)^2$

TABLE II

NORMALIZATION FRACTIONS

	2.01 BeV/c	3.15 BeV/c	4.13 BeV/c	4.95 BeV/c
Beam Attentuation ϵ_1	.934	.939	.943	.945
Electron Contamination ϵ_2	.978	.978	.978	.978
μ^- Contamination ϵ_3	.962	.966	.975	.978
Counter Attenuation ϵ_4	.994	.994	.994	.994
Other Attenuation ϵ_5	.98	.98	.98	.98

TABLE III

MULTIPLE COULOMB SCATTERING IN THE HYDROGEN TARGET

	2.01 BeV/c	3.15 BeV/c	4.13 BeV/c	4.95 BeV/c
θ_{lab}	.06°	.036°	.027°	.023°

TABLE IV

MOMENTUM RESOLUTION

	2.01 BeV/c	3.15 BeV/c	4.13 BeV/c	4.95 BeV/c
ΔP	$\pm$.10(BeV/c)	$\pm$.11(BeV/c)	$\pm$.13(BeV/c)	$\pm$.15(BeV/c)

TABLE V

EXPERIMENTAL AND PREDICTED REPRESENTATIVE CROSS SECTIONS

	2.01 BeV/c	3.15 BeV/c	4.13 BeV/c	4.95 BeV/c
σ_R	5.1 $\pm$ .5 mb	5.1 $\pm$ .5 mb	4.5 $\pm$ .5 mb	4.2 $\pm$ .4 mb
σ_E	4.5 $\pm$ .5 mb	6.5 $\pm$ .7 mb	5.5 $\pm$ .6 mb	5.1 $\pm$ .5 mb
% σ_E/σ_R	-12%	27%	22%	21%

TABLE VI

2.01 BeV/c ELASTIC π^- + p SCATTERING DATA

$-t(\text{BeV/c})^2$	Cos θ^*	Elastic Events (π-μ decay sub.)	$\frac{d\sigma}{d\Omega}$ (mb/sr)	$\frac{d\sigma}{dt}$ $\left(\text{mb}/(\text{BeV/c})^2\right)$
.0008	.9995	18.47 (7.53)	628.38±196.98	2598.35±814.51
.0021	.9986	10.27 (22.73)	30.39± 22.09	125.66± 91.34
.0046	.9970	29.0	17.36± 3.22	71.78± 13.31
.0076	.9950	38.0	16.55± 2.68	68.43± 11.08
.0106	.9930	40.0	16.89± 2.67	69.84± 11.04
.0144	.9905	70.0	19.77± 2.36	81.75± 9.76
.0190	.9875	44.0	12.71± 1.92	52.56± 7.94
.0236	.9845	39.0	11.82± 1.89	48.88± 7.82
.0289	.9810	48.0	11.84± 1.71	48.96± 7.07
.0350	.9770	39.0	10.83± 1.73	44.78± 7.15
.0418	.9725	27.0	6.85± 1.32	28.32± 5.46
.0532	.9650	58.0	9.01± 1.18	37.26± 4.87
.0684	.9550	35.0	7.07± 1.20	29.23± 4.96
.0911	.9400	54.0	6.98± 0.95	28.86± 3.92

TABLE VII

3.15 BeV/c ELASTIC π^- + p SCATTERING DATA

$-t(\text{BeV/c})^2$	Cos θ^*	Elastic Events	$\frac{d\sigma}{d\Omega}$ (mb/sr)	$\frac{d\sigma}{dt}\left(\text{mb}/(\text{BeV/c})^2\right)$
.0041	.99840	4.0	26.40±13.20	64.72±32.36
.0064	.99750	9.0	21.45± 7.15	52.59±17.53
.0090	.99650	20.0	28.61± 6.40	70.15±15.69
.0115	.99550	14.0	15.17± 4.06	37.19± 9.95
.0147	.99425	26.0	16.06± 3.15	39.38± 7.72
.0186	.99275	33.0	18.58± 3.23	45.55± 7.00
.0224	.99125	36.0	19.77± 3.30	48.47± 8.10
.0263	.98975	35.0	19.02± 3.22	46.63± 7.89
.0308	.98800	43.0	17.47± 2.66	42.83± 6.52
.0359	.98600	43.0	17.50± 2.67	42.91± 6.55
.0410	.98400	46.0	18.83± 2.80	46.17± 6.87
.0461	.98200	29.0	12.00± 2.23	29.42± 5.47
.0519	.97975	45.0	15.18± 2.26	37.19± 5.54
.0583	.97725	33.0	11.47± 2.00	28.12± 4.90
.0647	.97475	34.0	12.30± 2.11	30.16± 5.17
.0711	.97225	22.0	8.338± 1.78	20.44± 4.36
.0782	.96950	31.0	10.31± 1.85	25.28± 4.54
.0859	.96650	19.0	6.789± 1.57	16.65± 3.82
.0942	.96325	32.0	10.55± 1.86	25.87± 4.56
.1032	.95975	20.0	7.123± 1.59	17.46± 3.90
.1128	.95600	22.0	7.414± 1.58	18.18± 3.87
.1230	.95200	21.0	7.658± 1.71	18.78± 4.19
.1346	.94750	25.0	7.939± 1.59	19.46± 3.90
.1474	.94250	16.0	5.526± 1.63	13.55± 4.00

TABLE VIII

4.13 BeV/c ELASTIC π^- + p SCATTERING DATA

$-t(\text{BeV/c})^2$	Cos θ^*	Elastic Events	$\frac{d\sigma}{d\Omega}$ (mb/sr)	$\frac{d\sigma}{dt}$ $\left(\text{mb/(BeV/c)}^2\right)$
.0104	.9970	59.0	46.12±6.00	83.52±10.87
.0191	.9945	91.0	23.69±2.48	42.90± 4.49
.0312	.9910	141.0	20.64±1.74	37.38± 3.15
.0468	.9865	161.0	17.62±1.39	31.91± 2.52
.0642	.9815	117.0	12.99±1.20	23.52± 2.17
.0833	.9760	141.0	13.47±1.12	24.39± 2.05
.1041	.9700	108.0	10.92±1.05	19.78± 1.90
.1266	.9635	82.0	7.755±0.856	14.04± 1.55
.1457	.9580	45.0	8.099±1.21	14.67± 2.19

TABLE IX

4.95 BeV/c ELASTIC π^- + p SCATTERING DATA

$-t(\text{BeV/c})^2$	Cos θ^*	Elastic Events	$\frac{d\sigma}{d\Omega}$ (mb/sr)	$\frac{d\sigma}{dt}$ $\left(\text{mb/(BeV/c)}^2\right)$
.0148	.9965	54.0	33.53±4.56	49.79±6.77
.0275	.9935	79.0	23.24±2.61	34.51±3.88
.0423	.9900	113.5	19.72±1.85	29.28±2.75
.0614	.9855	113.0	14.72±1.38	21.86±2.05
.0847	.9800	125.5	13.75±1.23	20.42±1.83
.1122	.9735	114.0	11.01±1.03	16.35±1.53
.1373	.9676	67.0	9.658±1.18	14.34±1.75

TABLE X

COEFFICIENTS OF THE CURVE FIT AND COMPARISONS

$$\left(\frac{d\sigma}{d\Omega} = \frac{A}{t^2} - \frac{B}{t} + Ce^{Dt}\right)$$

Lab Momentum BeV/c	A $\left(10^{-4}(\text{BeV/c})^4 \text{ mb/sr}\right)$	B $\left(10^{-2}(\text{BeV/c})^2 \text{ mb/sr}\right)$	C (mb/sr)	D $\left((\text{BeV/c})^2\right)^{-1}$	D_ $(10^{-14} \text{ cm}/\sqrt{\text{sr}})$	Source
2.01	1.706 ± 1.274	- 1.795 ± 4.450	16.79 ± 3.71	11.31 ± 2.80	-2.173 ± 5.447	(1)
	0.647	---	---	---	---	(2)
	---	---	15.76 ± 0.18	9.64 ± 0.92	---	(3)
	---	-0.786	15.99	---	-1.545	(4)
3.15	1.091 ± 5.078	- 1.119 ± 11.141	22.34 ± 5.70	9.79 ± 1.69	-1.693 ± 17.310	(1)
	1.080	---	---	---	---	(2)
	---	---	21.0 ± 1.3	7.9 ± 0.3	---	(5)
	---	-1.975	22.51	---	-3.003	(4)
4.13	38.93 ± 25.96	-21.90 ± 31.89	29.78 ± 10.64	8.643 ± 1.410	-5.550 ± 5.851	(1)
	1.457	---	---	---	---	(2)
	---	---	27.6 ± 1.8	8.4 ± 0.3	---	(5)
	---	-2.441	27.11	---	-3.193	(4)
4.95	---	---	29.48 ± 2.64	8.95 ± 1.15	---	(1)
	---	---	32.5 ± 2.4	7.8 ± 0.3	---	(5)
	---	---	30.82	---	---	(4)

(1) This experiment.
(2) Coulomb scattering.
(3) Damouth.
(4) Dispersion calculations, Coulomb scattering, and optical theorem.
(5) Ting.

TABLE XI

PEARSON $P(\chi^2)$ VALUES FOR THE FITTED CURVES

	2.01 BeV/c	3.15 BeV/c	4.13 BeV/c	4.95 BeV/c
$P(\chi^2)$	<.01	.80	.80	.50

TABLE XII

$\pi^{\pm}$ + p FORWARD ELASTIC DISPERSION CALCULATIONS

(Values are in the center-of-mass)

T(BeV)	$D_-(10^{-14}$ cm/$\sqrt{sr})$	$D_+(10^{-14}$ cm/$\sqrt{sr})$	$D^{(-)}(10^{-14}$ cm/$\sqrt{sr})$
1.005	-3.72	-0.80	-1.96
1.105	-2.92	-0.25	-1.34
1.205	-2.22	-0.38	-0.92
1.305	-1.97	-1.64	-0.18
1.455	-2.02	-3.71	0.84
1.505	-1.99	-4.23	1.12
1.555	-1.86	-4.83	1.48
1.605	-1.68	-5.36	1.84
1.705	-1.52	-4.69	1.58
1.805	-1.48	-4.10	1.31
1.875	-1.54	-3.78	1.12
1.905	-1.63	-3.68	1.02
2.005	-1.92	-3.35	0.71
2.205	-2.54	-3.09	0.28
2.405	-2.71	-3.58	0.43
2.605	-2.84	-3.98	0.57
2.805	-2.92	-4.13	0.60
2.995	-2.99	-4.16	0.58
3.013	-3.00	-4.15	0.58
3.250	-3.05	-4.14	0.54
3.363	-3.09	-4.14	0.52
3.863	-3.18	-4.00	0.40
3.993	-3.19	-3.97	0.39
4.812	-3.26	-3.85	0.30
4.862	-3.26	-3.85	0.29
5.862	-3.36	-3.71	0.19

TABLE XII (Concluded)

T(BeV)	$D_-(10^{-14}$ cm/$\sqrt{sr})$	$D_+(10^{-14}$ cm/$\sqrt{sr})$	$D^{(-)}(10^{-14}$ cm/$\sqrt{sr})$
6.862	-3.43	-3.71	0.14
7.862	-3.47	-3.72	0.12
8.861	-3.50	-3.71	0.11
9.861	-3.50	-3.67	0.08
10.861	-3.53	-3.65	0.06
11.861	-3.53	-3.62	0.04
12.861	-3.51	-3.57	0.03
13.861	-3.51	-3.53	0.01
14.861	-3.49	-3.49	-0.01
15.861	-3.47	-3.44	-0.02
16.861	-3.45	-3.39	-0.03
17.861	-3.44	-3.35	-0.05
18.861	-3.41	-3.30	-0.06
19.861	-3.38	-3.25	-0.07
21.861	-3.31	-3.13	-0.09
23.861	-3.23	-3.02	-0.11
24.860	-3.19	-2.97	-0.12
27.000	-3.09	-2.84	-0.13
29.000	-2.95	-2.69	-0.14

TABLE XIII

RATIOS OF REAL TO IMAGINARY PART
OF THE π^- + p FORWARD SCATTERING AMPLITUDE

Source	2.01 BeV/c	3.15 BeV/c	4.13 BeV/c
This Experiment	-.1700 ± .4268	-.1143 ± 1.1703	-.3397 ± .3668
Dispersion Calculations	-.1232	-.2039	-.1979

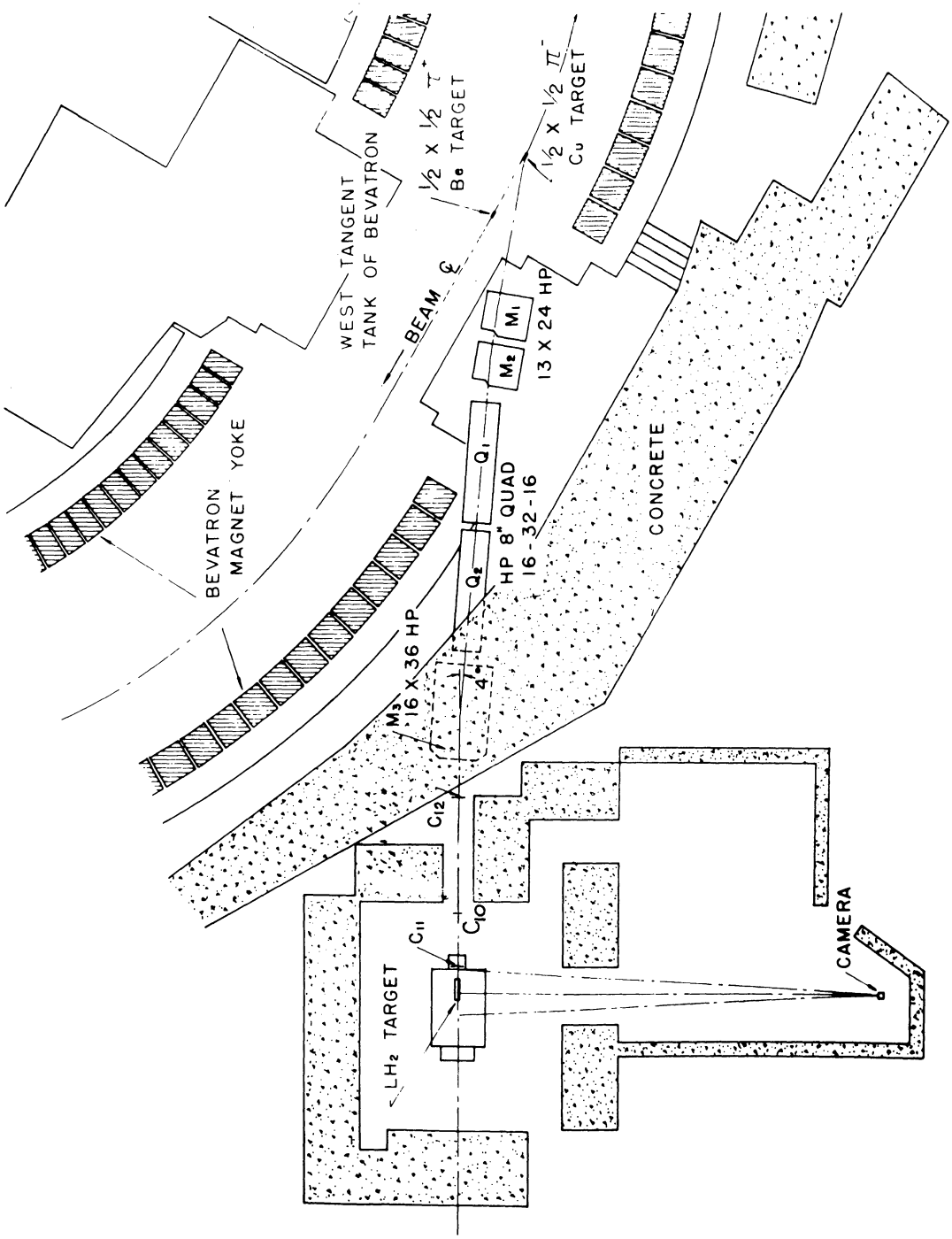

Fig. 1. Beam layout.

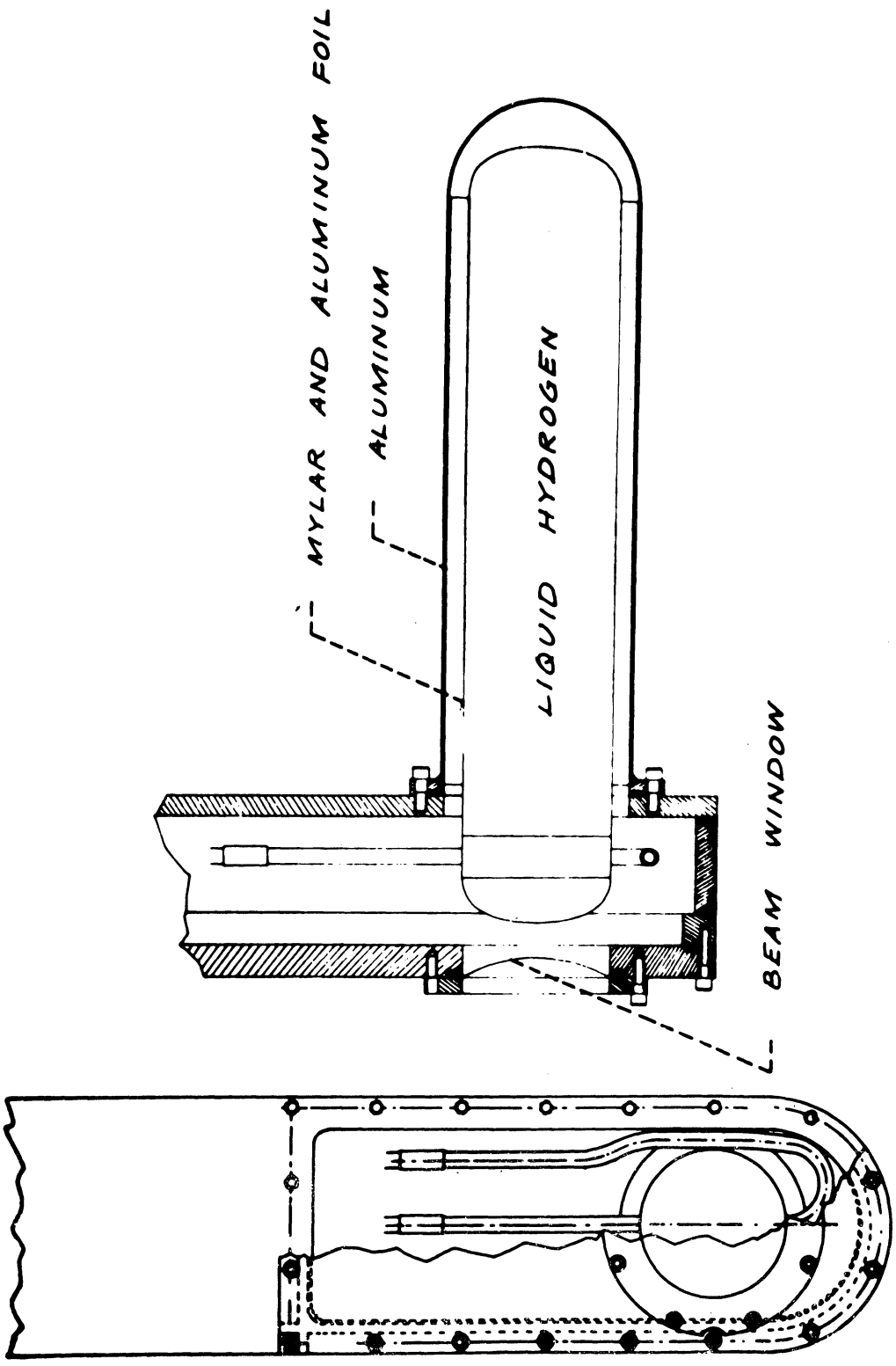

Fig. 2. Hydrogen target

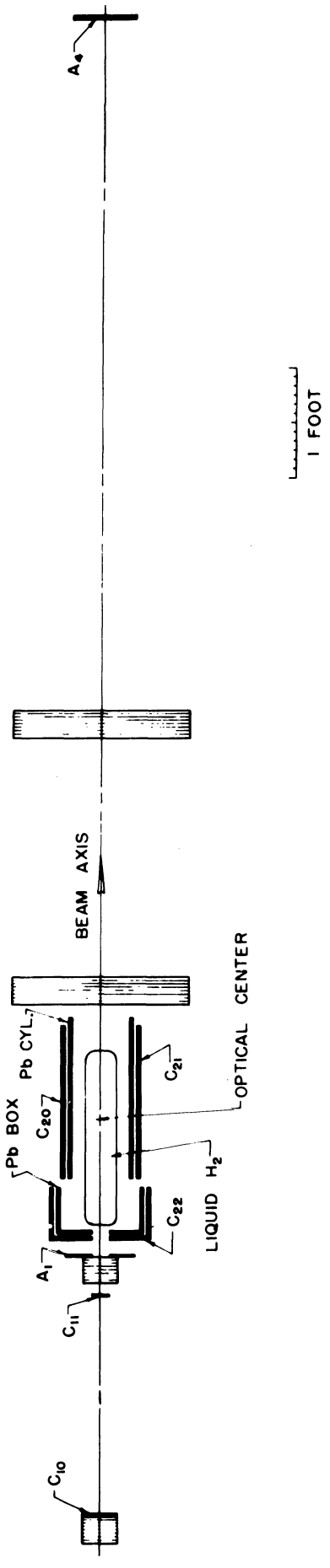

Fig. 3. Spark chambers and scintillation counters.

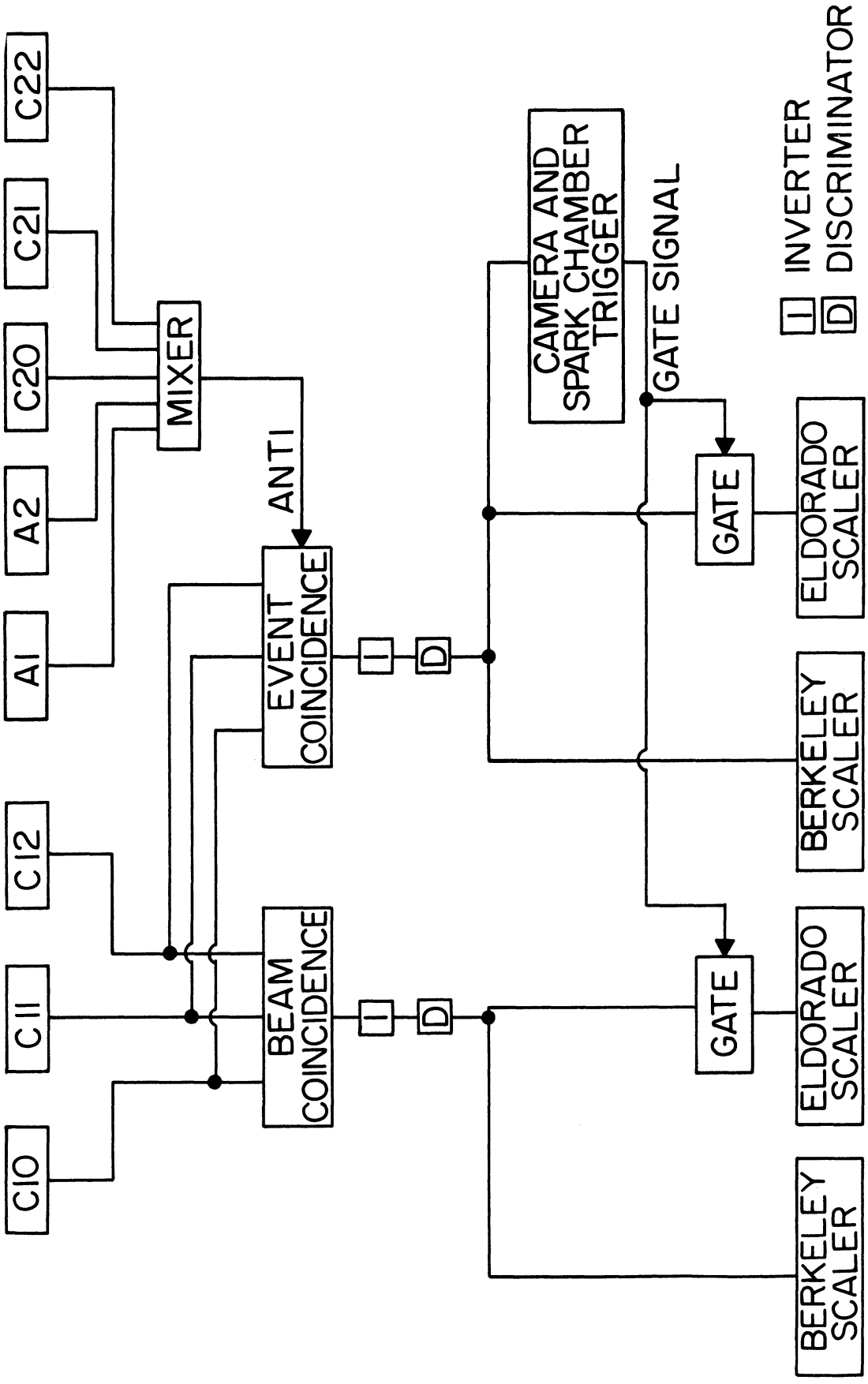

Fig. 4. Block diagram of the trigger system.

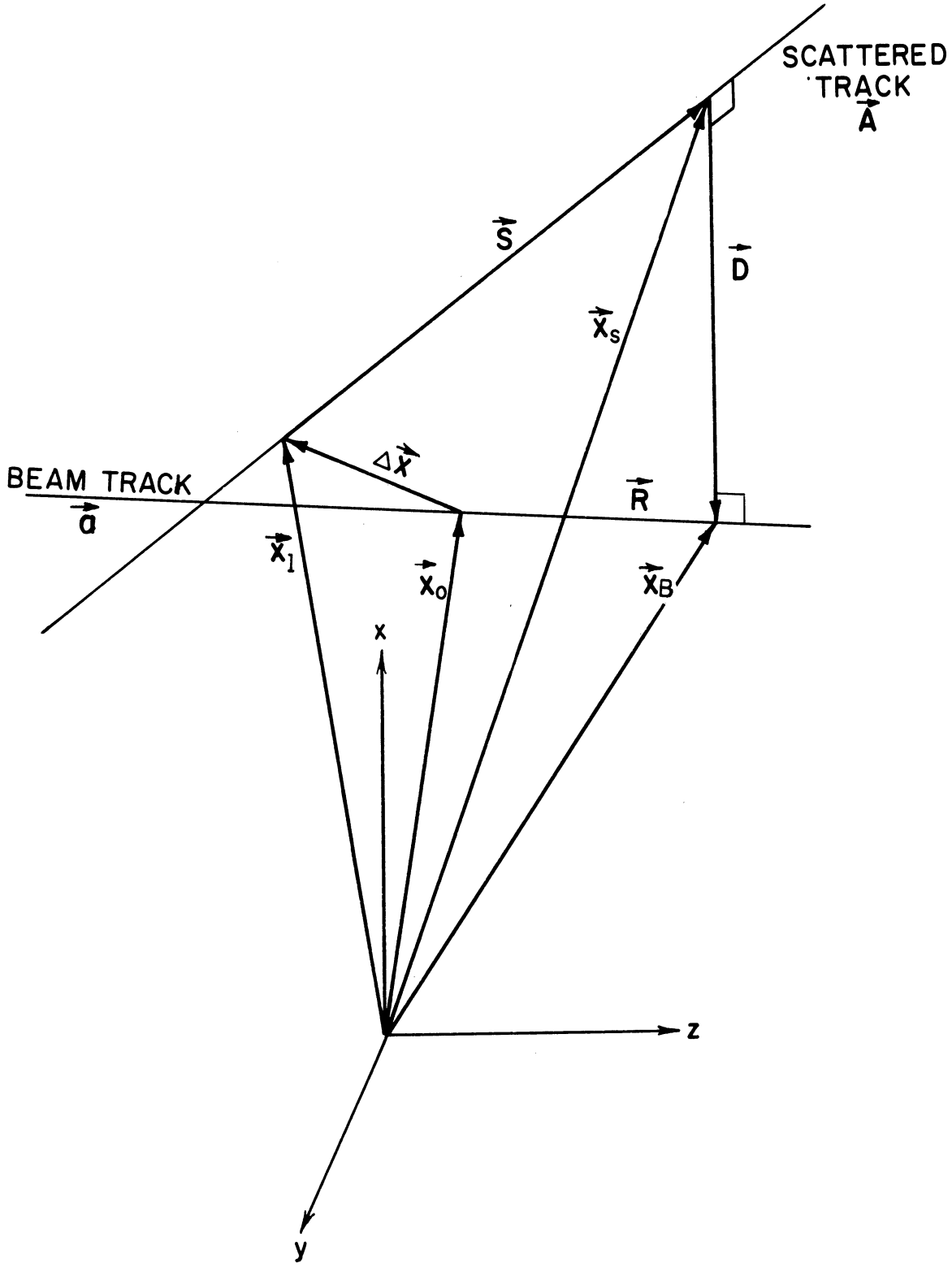

Fig. 5. Reconstruction of an event.

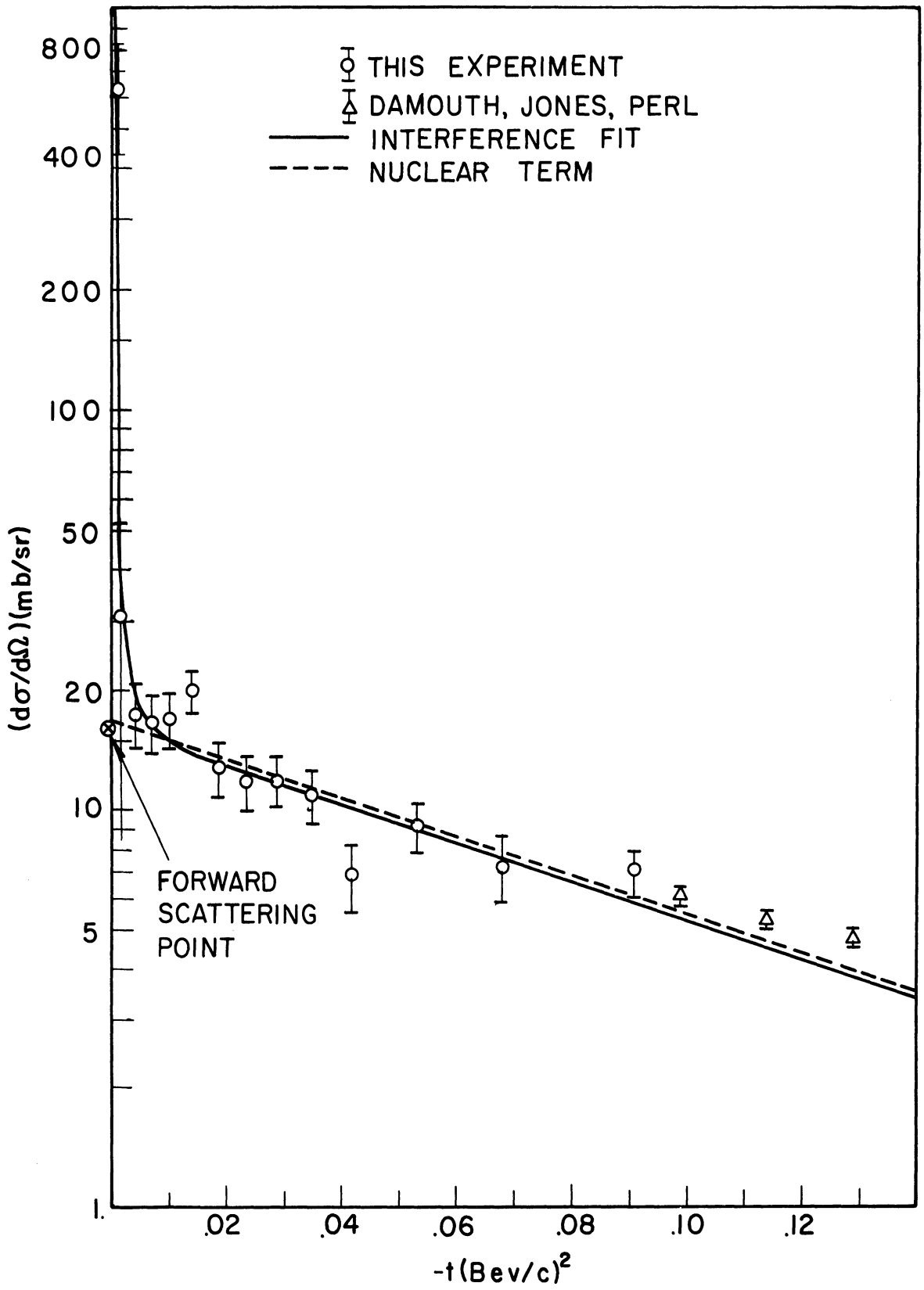

Fig. 6. π^- + p elastic differential cross section for 2.01 BeV/c.

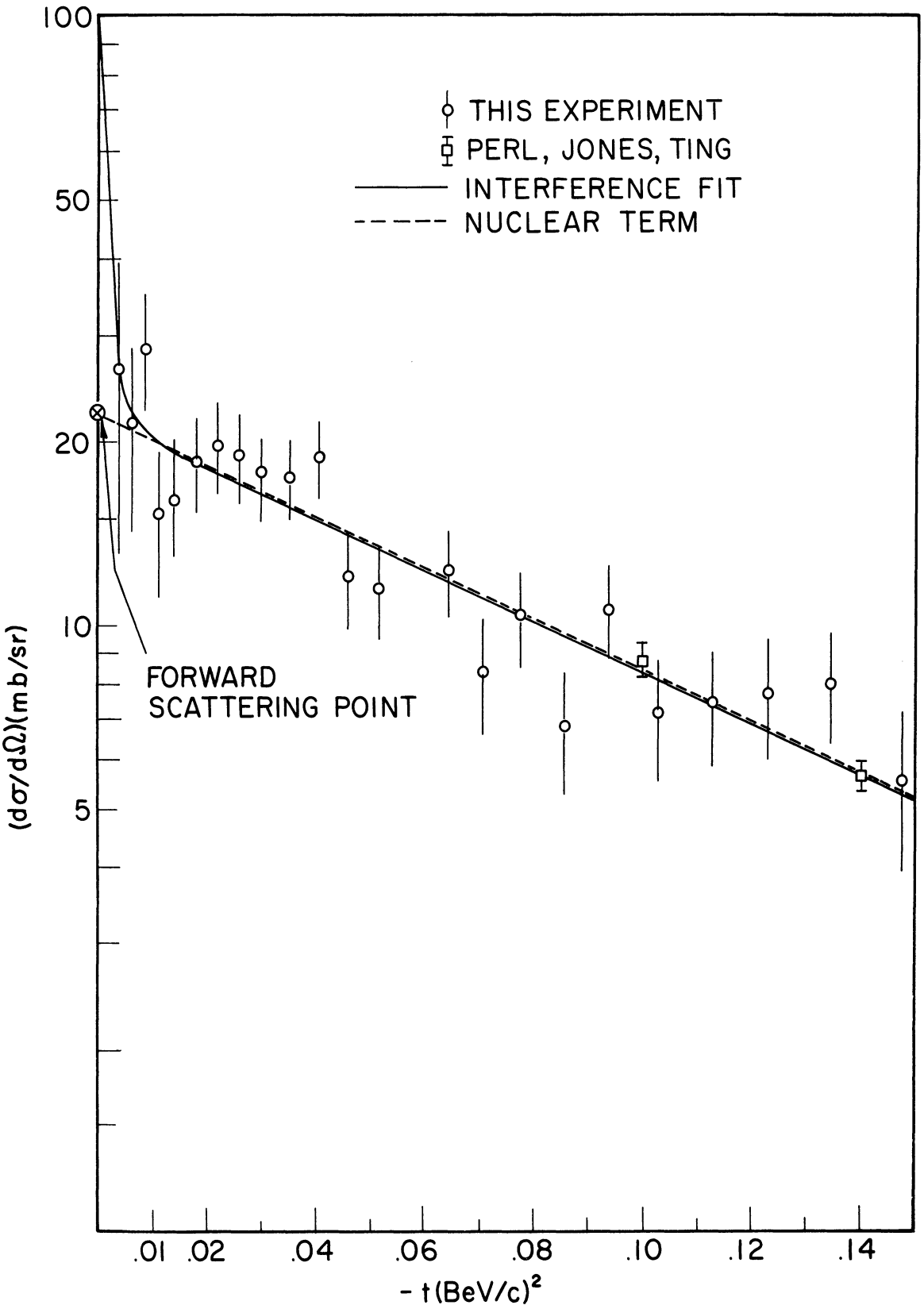

Fig. 7. π^- + p elastic differential cross section for 3.15 BeV/c.

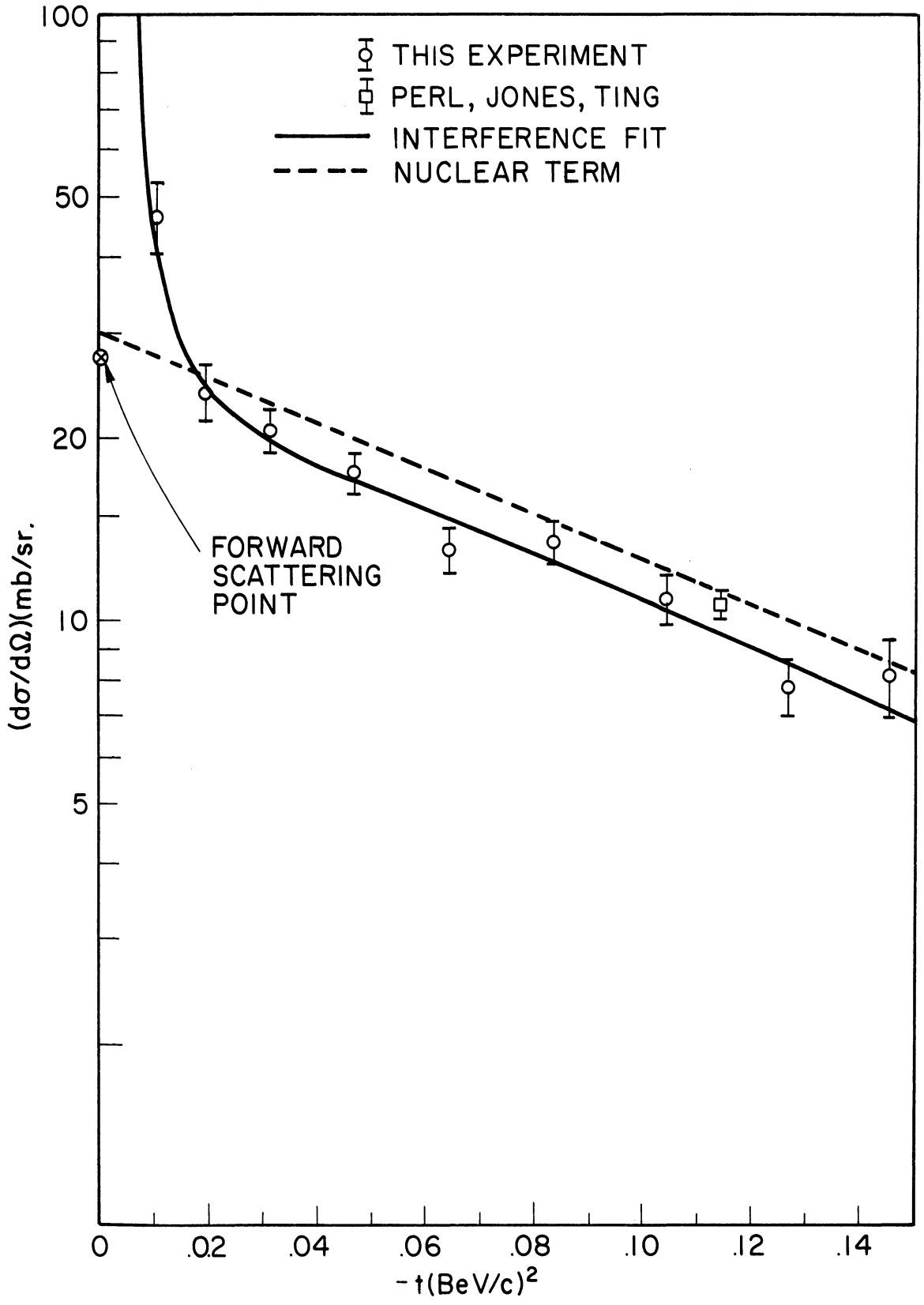

Fig. 8. π^- + p elastic differential cross section for 4.13 BeV/c.

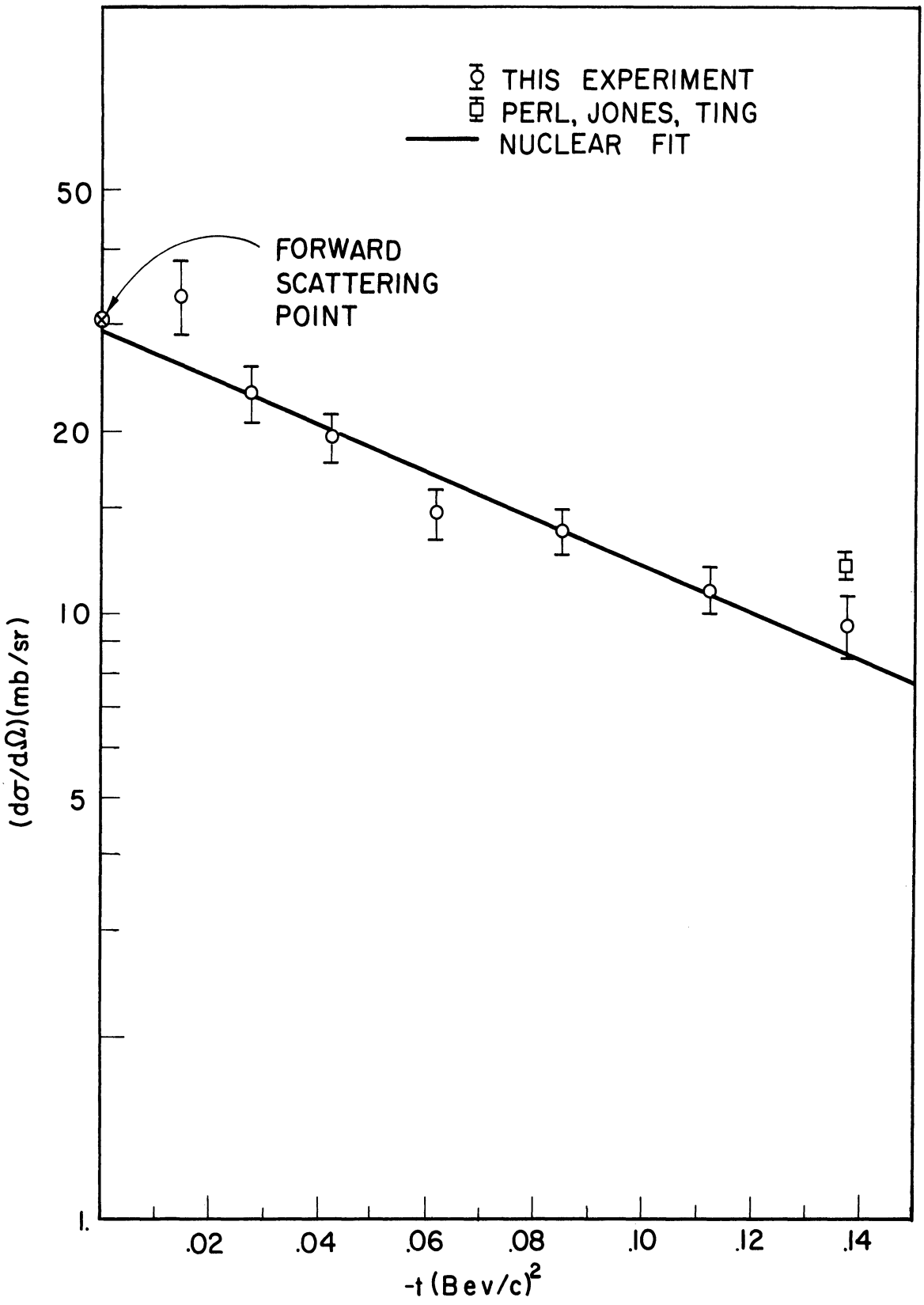

Fig. 9. π^- + p elastic differential cross section for 4.95 BeV/c.

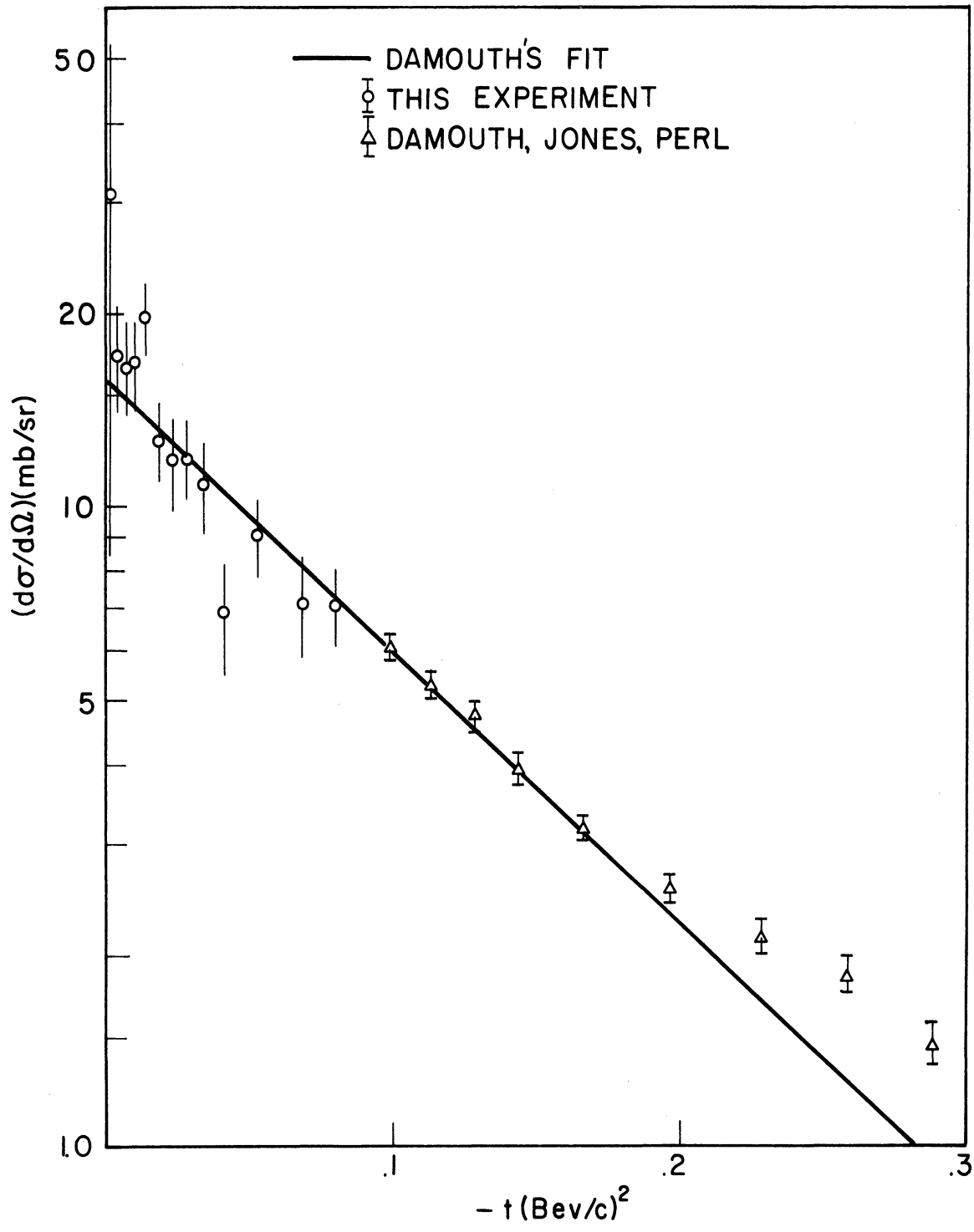

Fig. 10. Composite elastic results at 2.01 BeV/c.

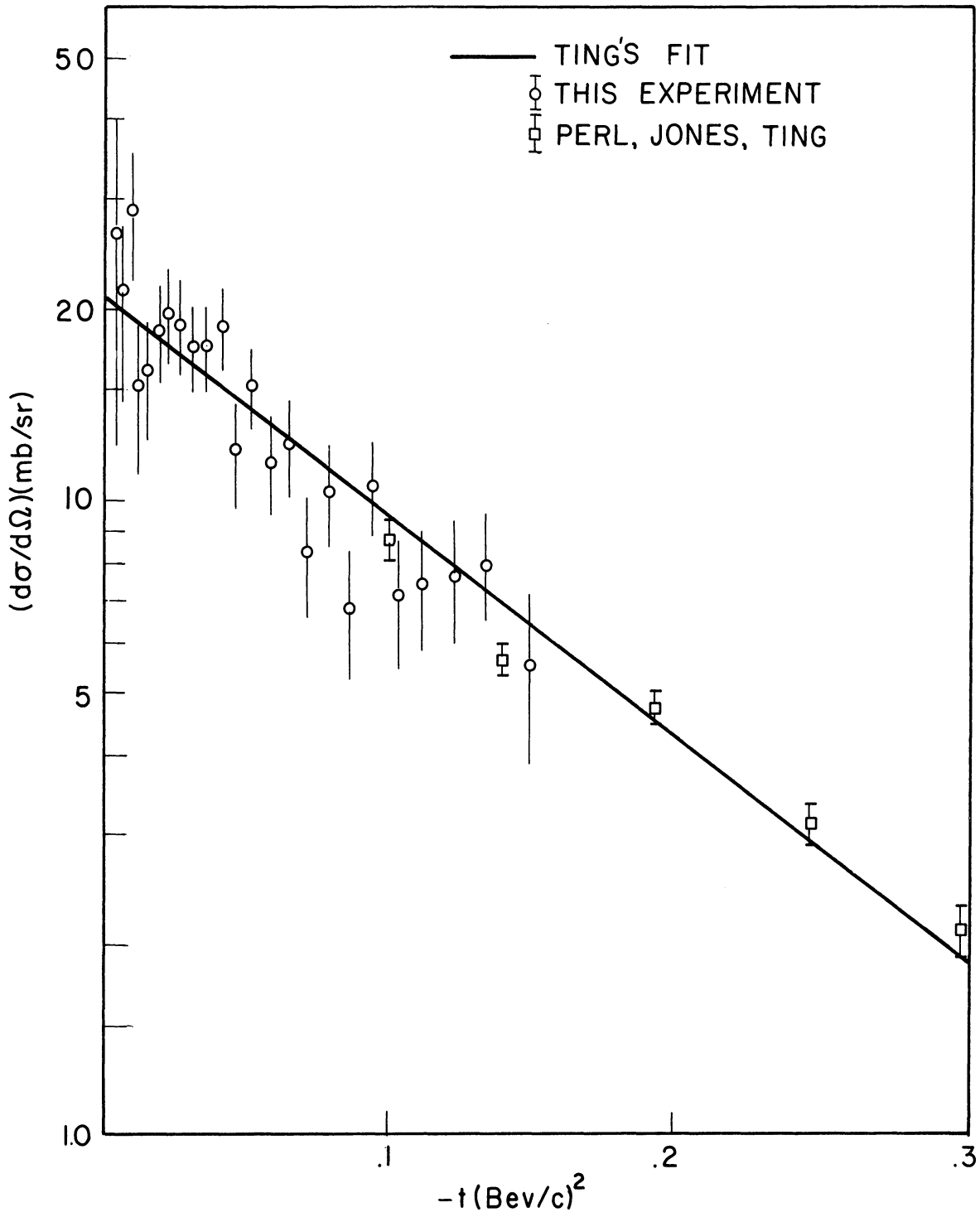

Fig. 11. Composite elastic results at 3.15 BeV/c.

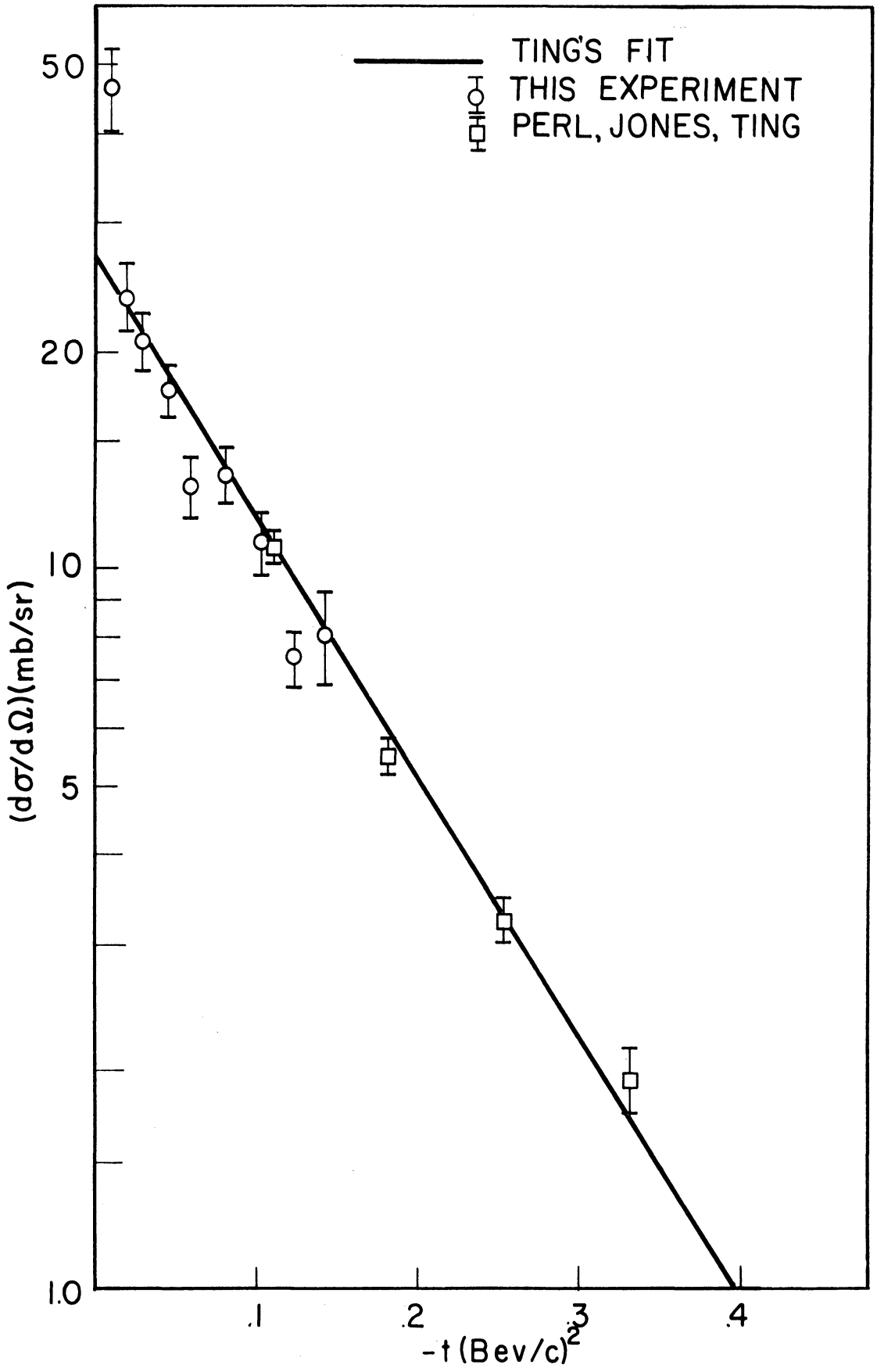

Fig. 12. Composite elastic results at 4.13 BeV/c.

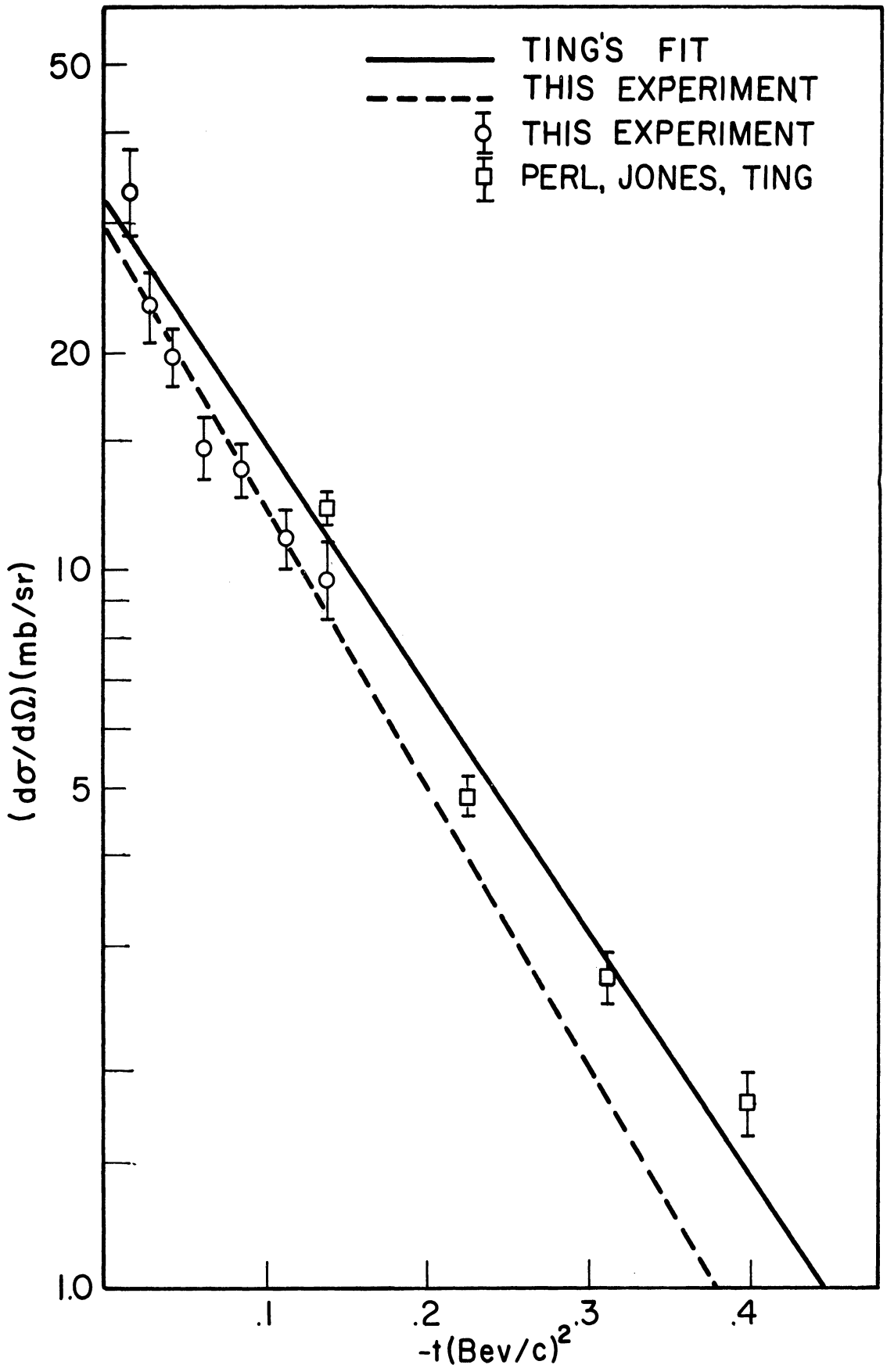

Fig. 13. Composite elastic results at 4.95 BeV/c.

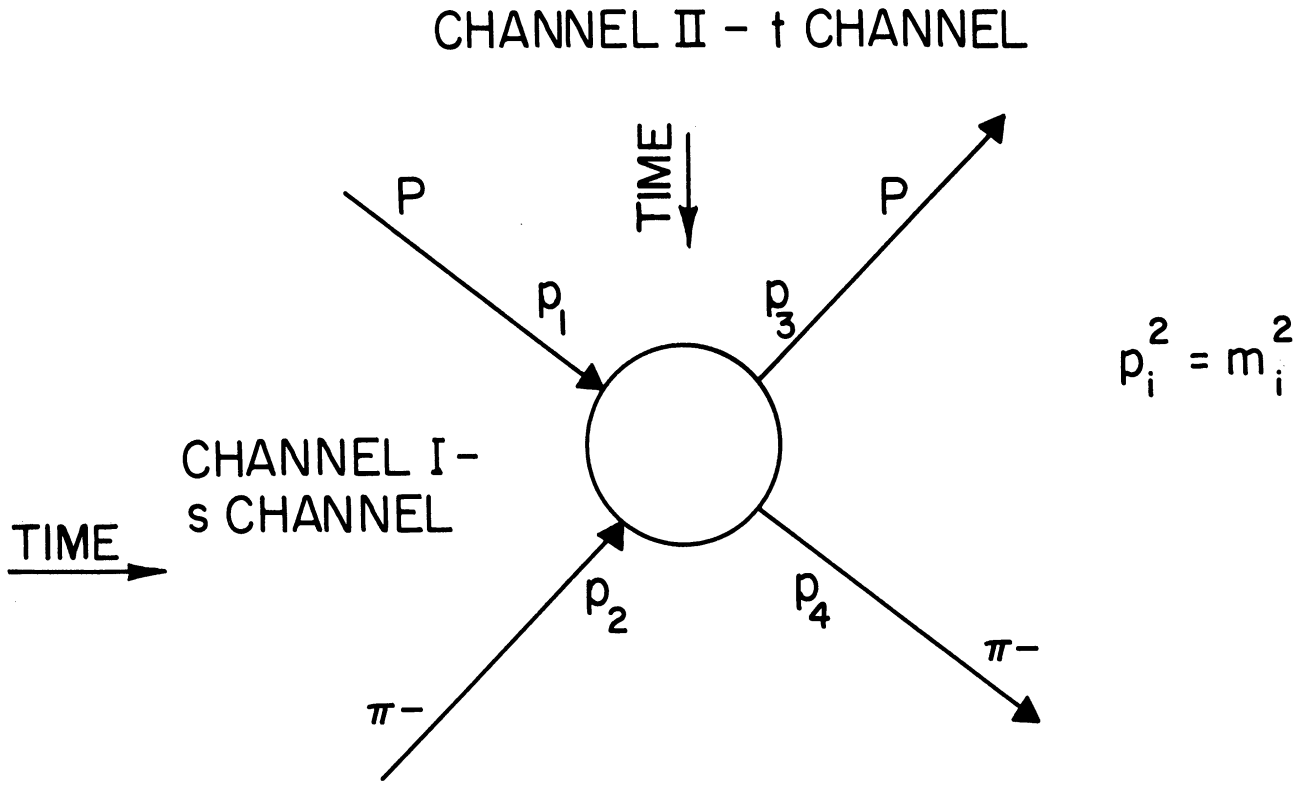

Fig. 14. π^- + p kinematics.

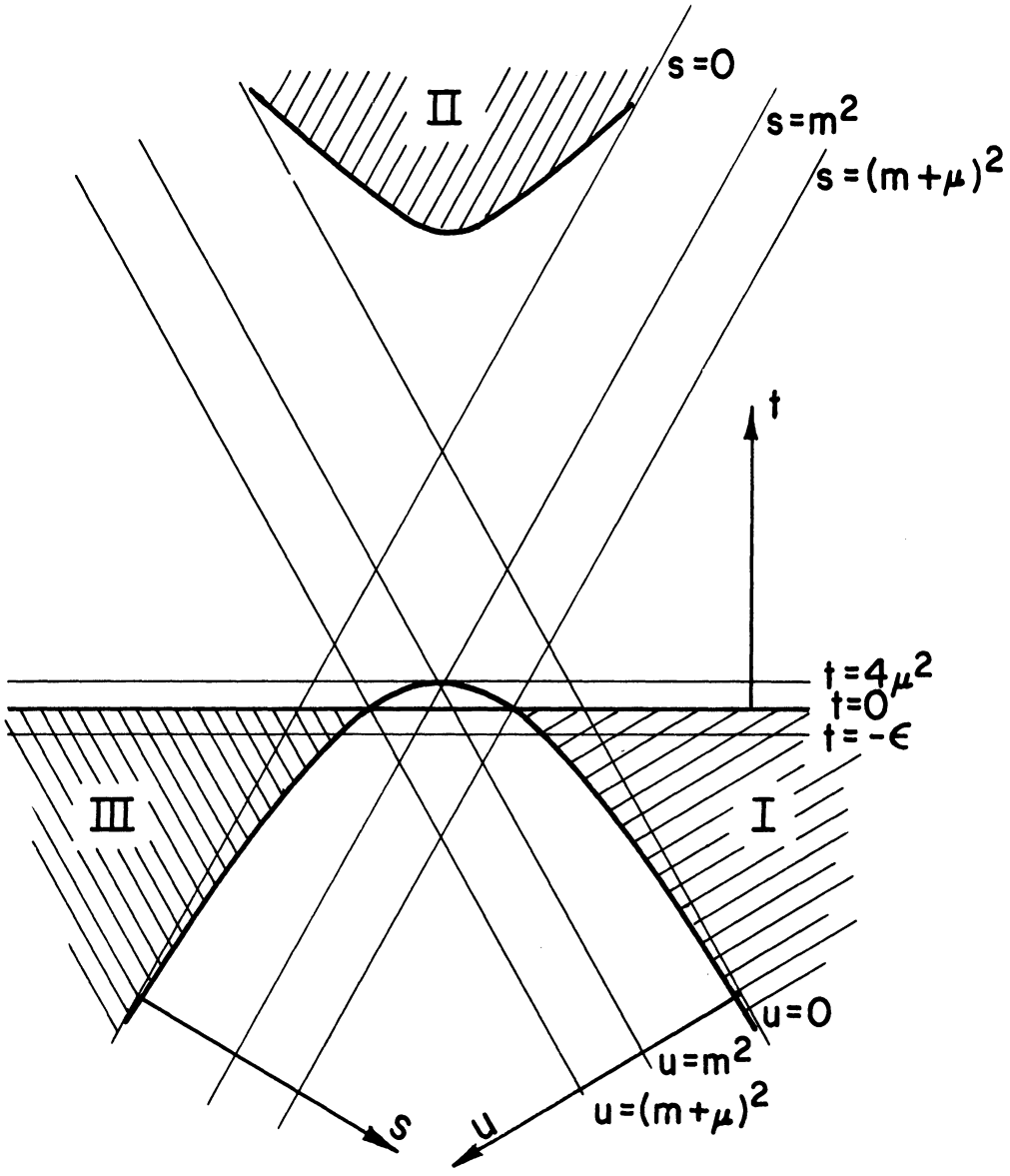

Fig. 15. Two-dimensional plot of the physical region.

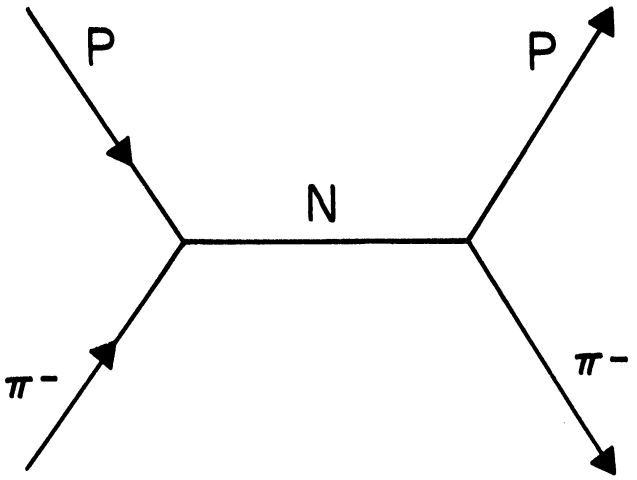

Fig. 16. π^- + p unphysical pole.

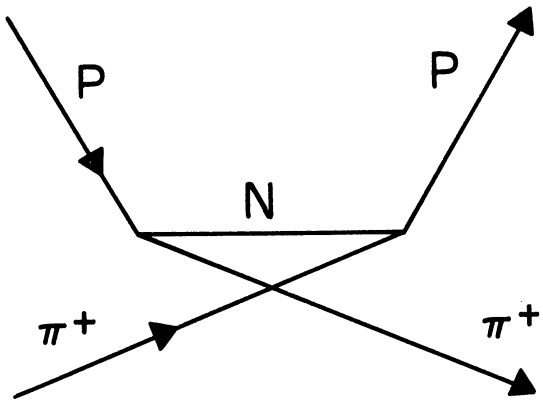

Fig. 17. π^+ + p unphysical pole.

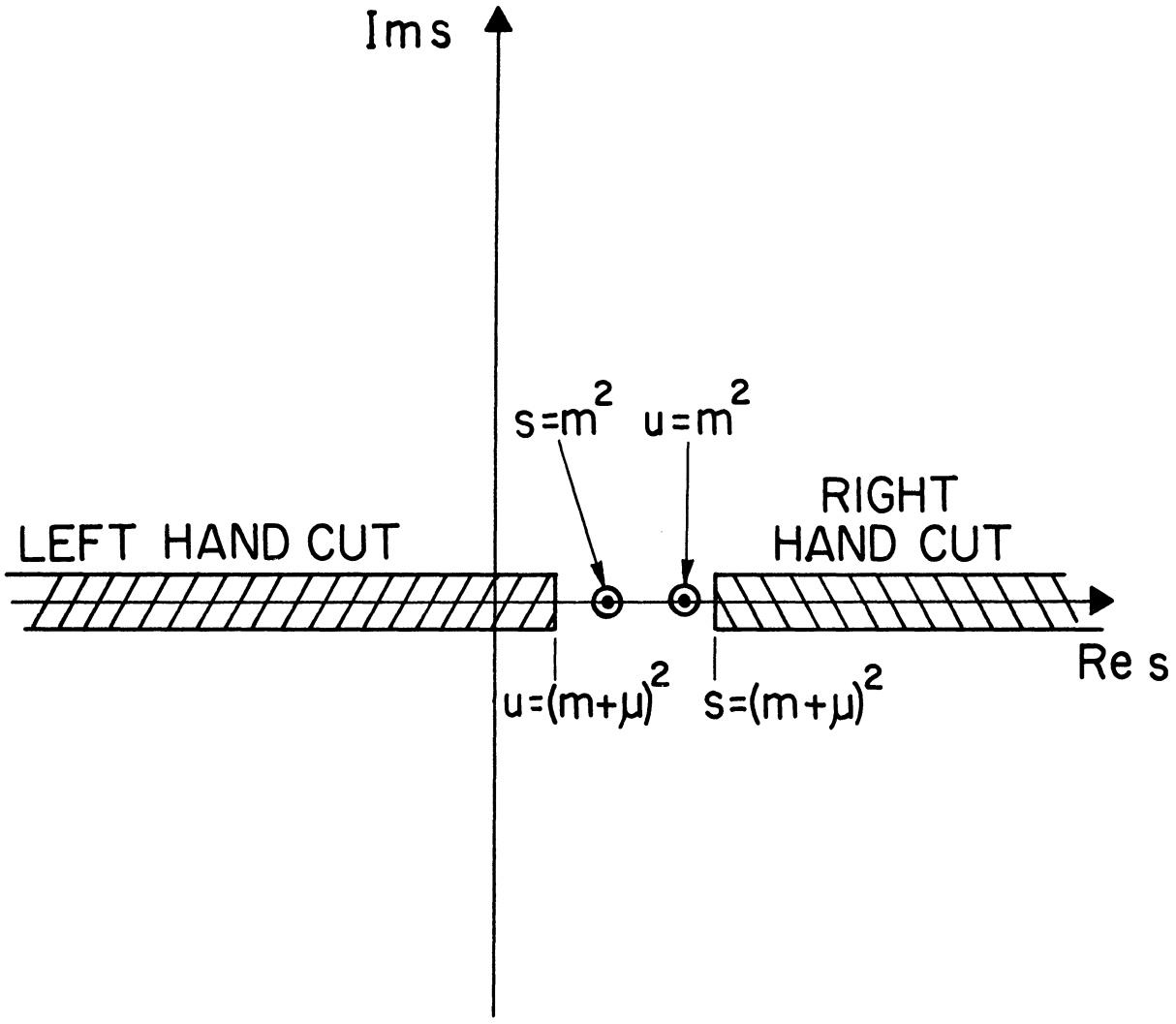

Fig. 18. A composite of the singularities.

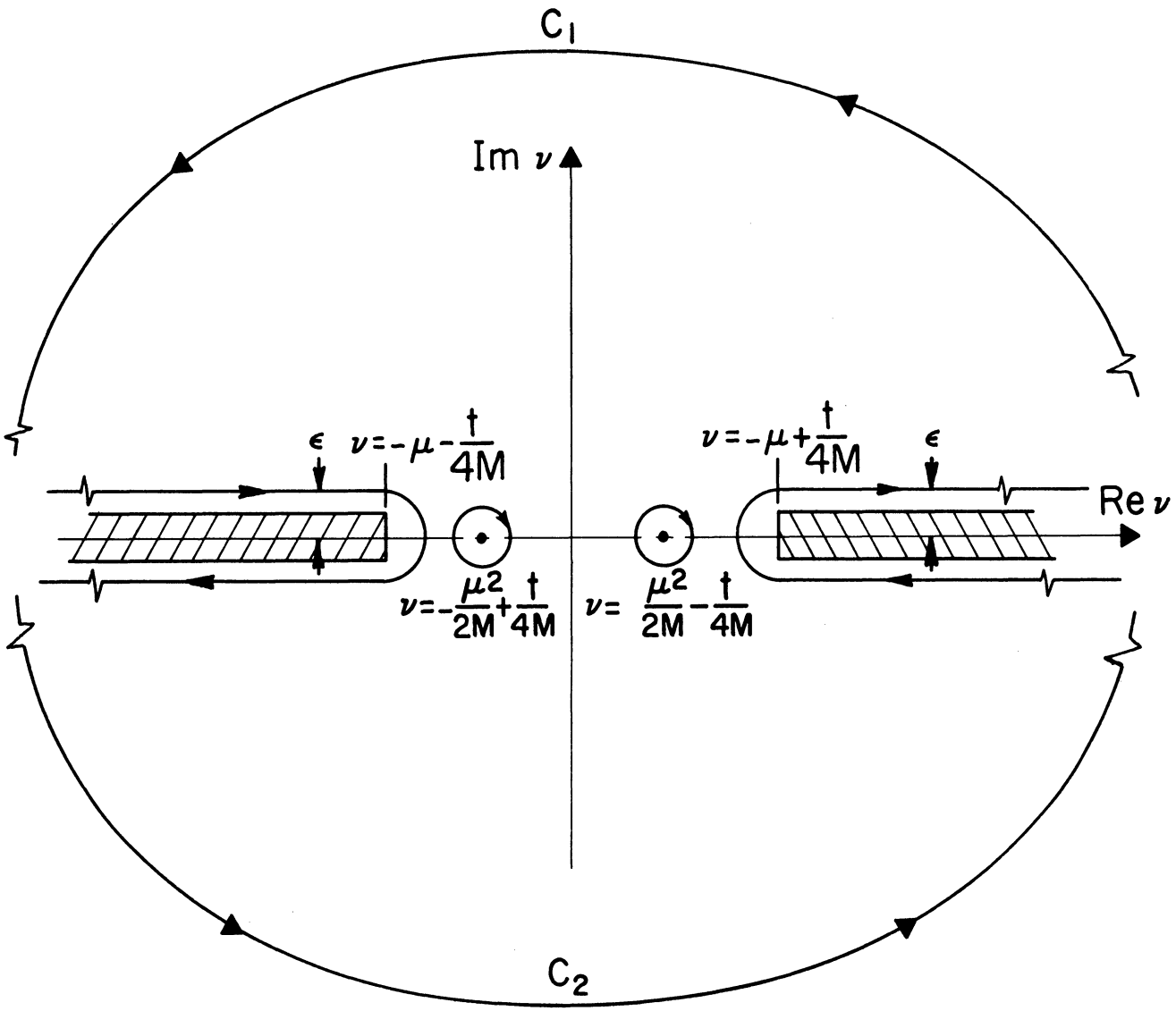

Fig. 19. The complex ν plane singularities and the path of integration.

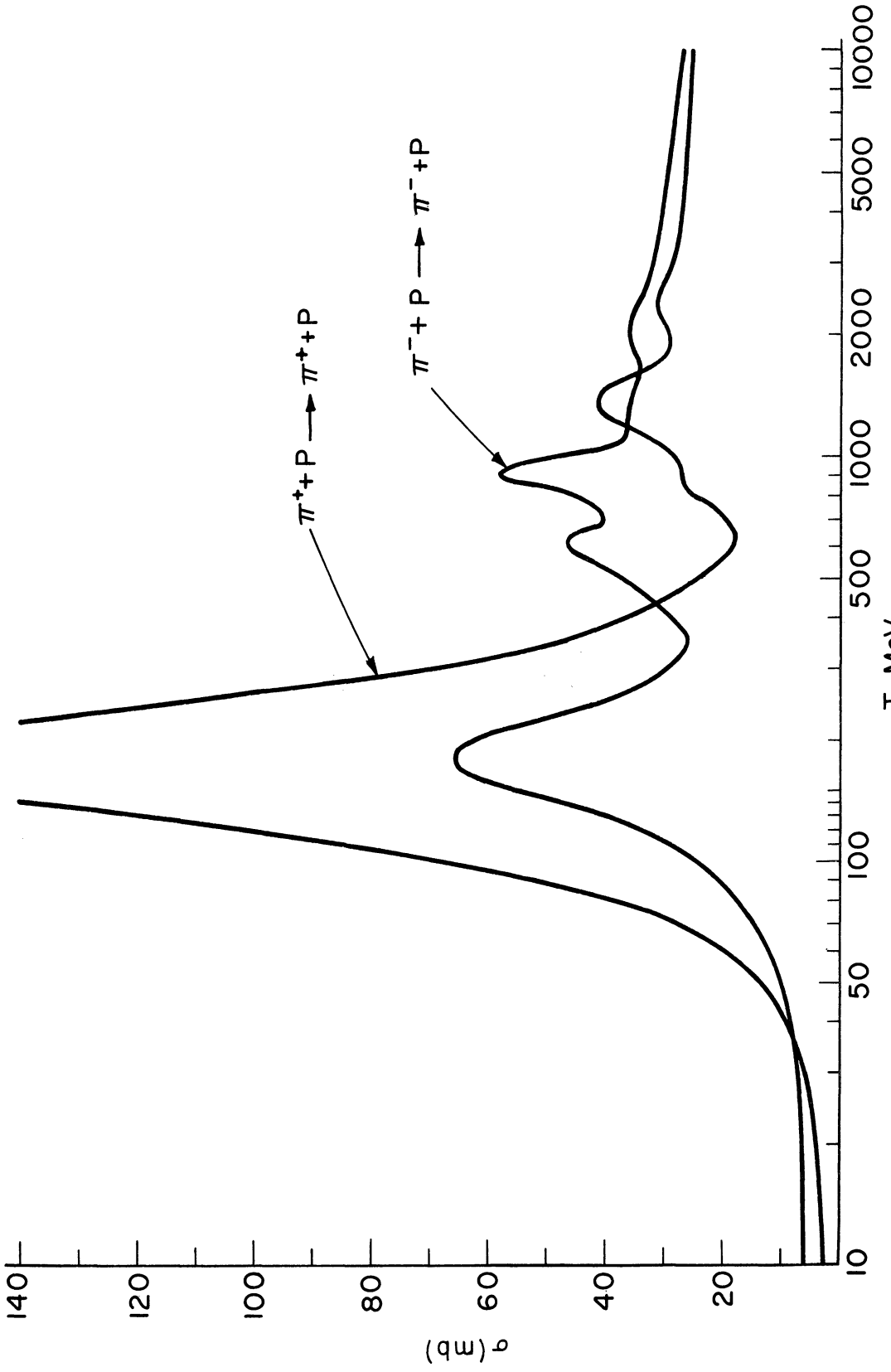

Fig. 20. $\pi^{\pm}$ + p total cross sections.

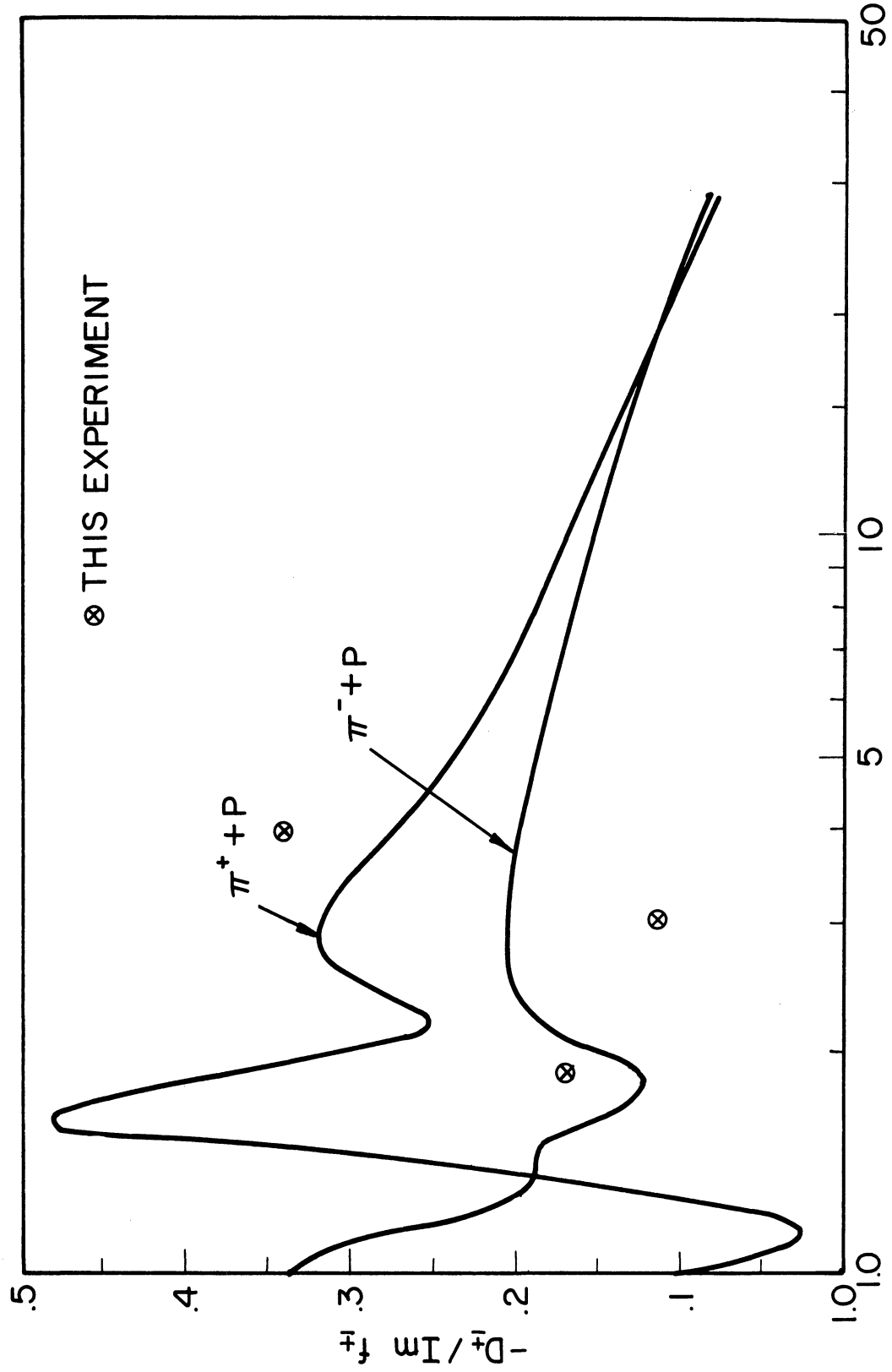

Fig. 21. The ratio of the real to the imaginary part of the elastic forward scattering amplitude.